MEASUREMENT SCIENCE REVIEW

Interferometric Surface Relief Measurements with Subnano/Picometer Height Resolution

Evgeny Sysoev[1], Sergey Kosolobov[2], Rodion Kulikov[1], Alexander Latyshev[2], Sergey Sitnikov[2], Ignat Vykhristyuk[1]

[1] *Technological Design Institute of Scientific Instrument Engineering, Siberian Branch of the Russian Academy of Sciences (TDI SIE SB RAS), 41, Russkaya str., 630058, Novosibirsk, Russia, evsml@mail.ru*
[2] *A.V. Rzhanov Institute of Semiconductor Physics, Siberian Branch of the Russian Academy of Sciences (ISP SB RAS), 13, Academika Lavrentieva Prospekt, 630090, Novosibirsk, Russia, kosolobov@isp.nsc.ru*

We present an optical interference system nanoprofiler MNP-1 designed for high-precision noncontact measurement of surface relief with subnanometer resolution (root mean square of measured values), based on partial scanning of interference signal. The paper describes the construction of the measurement system with Linnik interferometer and the algorithm for nanorelief surface reconstruction. Experimental measurement results of silicon sample with profile height of surface structure of one interatomic distance obtained by MNP-1 are shown. It was proposed to use an atomically smooth surface as the reference mirror in the interferometer MNP-1 that allowed us to measure monatomic steps of the presented silicon sample. Monatomic steps of 0.31 nm in height on silicon (111) surface were measured with resolution up to 5 pm.

Keywords: nanorelief, monatomic steps, low-coherence, white light interferometer, subnanometer resolution.

1. INTRODUCTION

Providing high resolution, when measuring the height of the surface relief, is an actual problem both in scientific research [1] and industrial production [2]. It is well known that the optical interference measuring techniques, especially white light interferometry, solve this problem, since the phase of the interference signal is very sensitive to small changes in the optical path difference between the interfering waves.

For precise measuring of surface nanorelief the well-known methods of phase shifting interferometry (PSI) are used. These methods are based on the phase calculation for the light scattered in the interferometer arms [3]. Typically, PSI measurement systems use Michelson, Linnik or Mirau interferometers [4], [5]. In this case for surface nanorelief measurement a scanning of interference signal phase is performed by changing the optical path difference of light between reference and measurement interferometer arms [6]. During the scanning process, a set of interferograms is recorded. The calculation of surface nanorelief height of measured sample is carried out by means of these interferograms at a known wavelength of used light source.

The recorded interferograms are the result of the interaction of two wavefronts formed by 'etalon', which is used as an interferometer reference surface and the surface of the measurement object. At the surface nanorelief calculation both surfaces 'etalon' and the measurement object influence the measurement results. The analysis of measurement results shows that measurement error is defined first of all by the quality of interferometer reference surface. When roughness of reference interferometer surface exceeds a height of surface relief of measurement sample a big error in the measurement results is observed.

As a rule, the interference systems designed for the measurement of surface nanorelief use flat optical mirrors made by spraying of Al on high quality glass substrate as an interferometer reference surface. The roughness of such mirrors is about 2 nm. To provide subnanometer height resolution the reference mirrors must have lesser roughness.

There is the approach to decrease the influence of reference mirror roughness. In the work [7] the authors proposed to carry out some uncorrelated measurements of supersmooth mirror and then to average the measurement results to get reference surface. Further, this reference surface is "subtracted" from subsequent measurements. This technique is similar to interferometer calibration by measuring the caliber surface. The surface relief of caliber is preliminary measured by a metrologically certified system. The data received in the process of interferometer calibration is also used to correct the measurement results.

Significant progress was achieved using the molecular beam epitaxy (MBE) technology for the formation of flat

smooth solid-state surfaces [8]. In this case there is a real opportunity to create the atomically smooth surface. By authors' opinion to decrease the influence of reference mirror roughness the most perspective is to use the atomically smooth surface as reference mirror of interferometer. The application of such reference mirror under the method of partial correlogram scanning allows us to decrease the error of surface nanorelief measurement and significantly improve resolution capability by height up to 5 picometers.

The paper describes the method of partial correlogram scanning assigned for measurement of 3D surface nanorelief and the nanoprofiler MNP-1. Experimental measurement results of silicon sample with height of surface structure of one monoatomic layer obtained by nanoprofiler MNP-1 are presented here. The results of using atomically smooth surface as the interferometer reference mirror in the measurement system MNP-1 to obtain the picometer resolution also are shown in the paper.

2. THE PARTIAL CORRELOGRAM SCANNING METHOD FOR SURFACE NANORELEIF MEASUREMENT

The principle of surface nanorelief measurement is based on the method of partial correlogram scanning and described in detail in [9]. According to this method the correlograms are registered for different parts of measurement surface as shown in Fig.1. The correlogram is the function of interference intensity depending on the phase changing. Height difference Δh between different surface parts leads to that the recorded correlograms have different phase shift $\Delta \Phi$ (Fig.1.). They are related by the following expression:

$$\Delta h = \frac{\Delta \Phi}{2\pi} \cdot \frac{\overline{\lambda}}{2},$$

where $\overline{\lambda}$ is the effective wavelength.
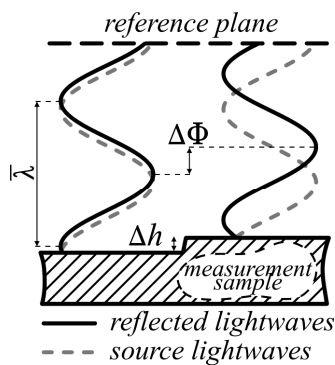
Fig.1. Measurement method: different phase shift of lightwaves reflected from the measurement sample.

At the measurement of surface nanorelief by this method only a part of correlogram (which includes 2-3 periods) is registered in each point. Correlograms are obtained in the process of changing the optical path difference between interfering lightwaves. The scanning process of phase is carried out with selected scanning step, for example, by piezoelectric transducer. Interferograms which are formed for each scanning step can be registered by multielement photodetector and then digitized and transmitted to personal computer. After the scanning process for each points of measurement area (these points correspond to photodetector elements) the correlograms are formed. For example, two correlograms which correspond to two points on the surface with different heights are shown in Fig.2.

Phase difference $\Delta \Phi$ between obtained correlograms is calculated from the following expression:

$$\Delta \Phi = \frac{\Delta n}{2N} \cdot 2\pi,$$

where $2N$ is the amount of scanning steps necessary for changing the optical path difference between interfering beams at half of effective wavelength, and Δn is the shift between correlograms (calculated in the number of scanning steps).
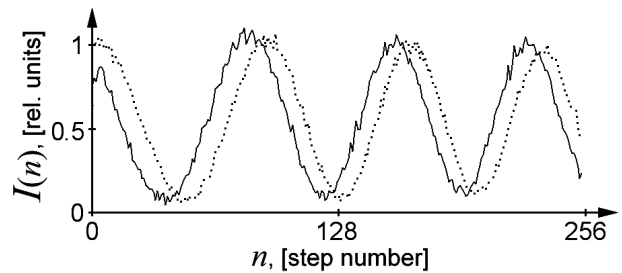
Fig.2. The correlograms for two different points of the surface: $I(n)$ is the light intensity, n is the number of scanning step.

The N and Δn values are calculated by the displacement of the first correlogram $I_1(n)$ relative to the second one $I_2(n)$. Displacement when the value of standard deviation reaches a minimum corresponds to the desired value of shift:

$$\sigma(\Delta n) = \sqrt{\frac{2}{K} \cdot \sum_{n=K/4}^{3K/4-1} \left[I_1(n) - I_2(n + \Delta n) \right]^2} \underset{\Delta n \in [-K/4, K/4]}{\to} \min,$$

where K=256 is the number of registered interferograms.
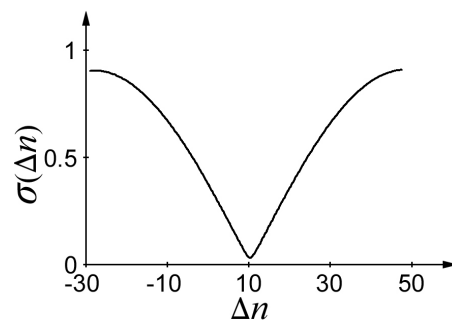
Fig.3. The calculation of shift between two correlograms: $\sigma(\Delta n)$ is the standard deviation, Δn is the shift between two correlograms.

At the definition of *N* value the second correlogram is a copy of the first one but inverted in intensity. In the case of definition of Δ*n* value the two correlograms corresponding to different part of measured surface are used. The example of the dependence of standard deviation σ on assigned displacement at definition of Δ*n* value is shown in Fig.3.

The calculation of phase difference between all correlograms reconstructs the surface nanorelief.

A distinctive feature of the method of partial correlogram scanning is that the required scanning range is less than 1 µm and the scanning involves displacement of reference mirror only. This allows one to significantly increase the measurement speed and simplify the design of the microscope. Moreover, an absolute phase value is not used under the phase difference calculation. In the case of the absolute phase measurements the relief height is unambiguously defined in the phase variation range of 2π. The calculation of relief height by the method of partial correlogram scanning is based on calculation of phase variations. A priori, if we assume that the height difference between two neighbor parts of measured surface does not exceed $\overline{\lambda}/4$, then this method allows measuring the surface nanorelief height in the range limited by coherence length of the used light source. At that the ambiguity in the measurement of surface nanorelief arises only at a local height difference of $\pm\overline{\lambda}/4$. That feature allows avoiding the ambiguity of relief height calculation.

3. MNP-1 NANOPROFILER

Morphology of sample surface was analyzed by the method of partial correlogram scanning by means of nanoprofiler MNP-1 [10]. This measurement system was developed and produced at TDI SIE SB RAS. Nanoprofiler MNP-1 shown in Fig.4. consists of optomechanical module 1, electronic module 2, and computer 3 with specially designed software.
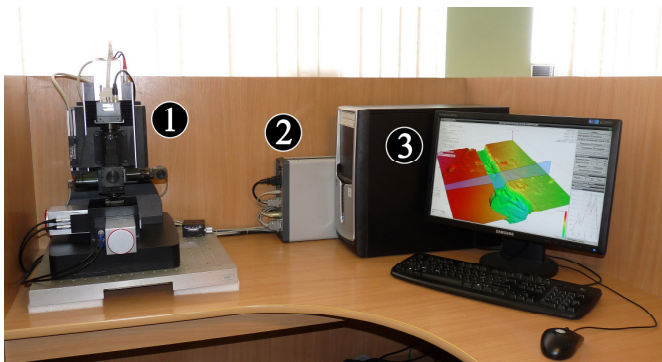
Fig.4. Nanoprofiler MNP-1: 1 – optomechanical module,
2 – electronic module, 3 – computer.

Detailed scheme of nanoprofiler MNP-1 is shown in Fig.5. Optomechanical module includes the base with horizontal *XY*-axes stage 5 and vertical *Z*-axis stage 4 fixed on holder. Stages controller installed inside the computer 3 operates the carriage position of XY-axes and Z-axis stages. Main part of

the interferometer 1 is mounted on the carriage of *Z*-axis stage 4. The carriage position of *Z*-axis stage is controlled by linear displacement sensor 14 connected to the electronic module 2. The computer 3 controls the light source 6, the piezoelectric transducer 9 and the power supply of CCD camera 15 by electronic module 2 via USB 2.0 interface. The CCD camera 15 registers images and through the frame grabber transmits them to the computer. To carry out the measurements the investigated object 13 is placed on *XY*-axes stage 5.

The interferometer was designed according to the scheme of Linnik micro-interferometer [11]. The light wave from a source of partially coherent light 6 (used LED) passes through a collimating objective 10 and gets onto the beam splitter cube 7, where it is divided by the amplitude into two parts. One part of light wave propagates in the reference arm, another one – in the measurement arm of interferometer. In the reference arm of the interferometer the light wave passes through the microobjective 12 and gets onto the surface of reference mirror 8 fixed on the piezoelectric transducer 9. Propagating in the measurement arm of the interferometer the light wave passes through the microobjective 11 and gets onto the surface of measurement object 13. The light partially scattered and reflected by the surfaces of reference mirror and measurement object is registered by matrix of the CCD camera 15. The interference phenomena are observed under the condition that the optical path difference of light between reference and measurement arms does not exceed the coherence length of the used light source.
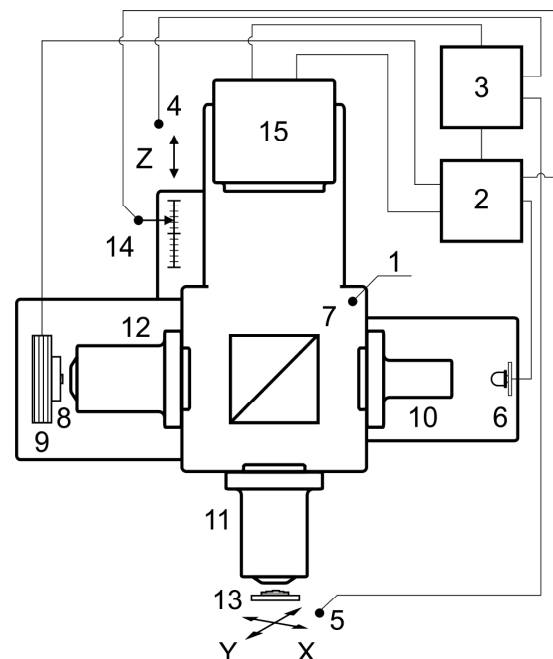
Fig.5. Scheme of nanoprofiler MNP-1: 1 – main part of interferometer, 2 – electronic module, 3 – PC, 4 – *Z*-axis stage, 5 – *XY*-axes stage, 6 – low coherence light source,
7 – beam splitter, 8 – reference mirror, 9 – piezoelectric transducer,
10 – collimating objective, 11-12 –micro objectives,
13 – measuring surface, 14 – linear displacement sensor,
15 – CCD-camera.

4. EXPERIMENTAL RESULTS OBTAINED BY MNP

In order to determine the height resolution of the interferometric system nanoprofiler MNP-1 a special surface of silicon sample was used. This measurement sample was designed at A.V. Rzhanov Institute of Semiconductor Physics, Siberian Branch of the Russian Academy of Sciences (ISP SB RAS). The investigated sample was prepared by thermal annealing of the silicon (111) crystal under ultrahigh vacuum conditions. After thermal annealing, the samples were evacuated from UHV (ultra-high vacuum) chamber and their morphology was analyzed at ambient conditions. Current sample of silicon crystal contains on the surface the structure of monoatomic steps with height in one atomic spacing of crystal lattice of silicon. The step height was measured by the producer using AFM (Solver P47H, Integra Aura, NT MDT) and was equal to 3.14 Å. The standard silicon cantilevers were used for profile measurements both in contact and in semi-contact modes at ambient condition. Fig.6. represents the measurement result, namely: the AFM-image (semi-contact mode) of the silicon surface on the area $80 \times 80\ \mu m^2$ with the atomic steps 0.31 nm in height, bounded two-dimensional "negative island".
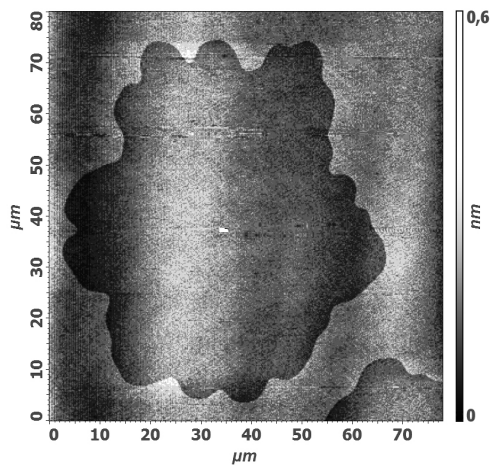
Fig.6. AFM-image $80 \times 80\ \mu m^2$ of silicon surface with negative island of monoatomic depth.

The measurements of proposed sample made by the nanoprofiler MNP-1 were carried out at the parameters of the measurement system which are given further. The microobjectives with magnification $20^\times$ and numerical aperture (*NA*) 0.4 were used in the reference and measurement arms of Linnik interferometer. As a light source in the interferometer we have applied the calibrated light source with effective wavelength 630 ± 0.5 nm. The calibration of light source was carried out by the spectrometer LINOS QWave with resolution ability of 0.5 nm. A preliminary calibration of the spectrometer was carried out by He-Ne laser with wavelength 632.9918 nm stabilized by Lamb dip with relative non-stability of optical frequency not more than 10^{-8}. Also, the value of wavelength can be changed by the optical scheme of interferometer. In work [12] was shown that the value of wavelength depends on NA. Estimated value of the wavelengths difference for used microobjectives $20^\times$ with NA = 0.4 and $\lambda = 630$ nm is less than 4 %. In case of measurement of monoatomic steps with height 3.14 Å it leads to insignificant systematic error.

CCD camera Hitachi KP-F120CL was used for interferograms registration. The camera pixel size is $6.45\ \mu m \times 6.45\ \mu m$. The pixel size in the measurement area is equal to $0.32\ \mu m \times 0.32\ \mu m$. The registration process of interferograms was performed by averaging of four frames.

Fig.7. shows results of the first set of measurements. They were performed by the nanoprofiler MNP-1. In the reference arm of MNP-1 interferometer an optical flat mirror made by vacuum spraying of Al on high quality glass substrate was used. Three-dimensional surface relief reconstruction (Fig.7.a)) and corresponding plot of height distribution (histogram) for the sample region (Fig.7.b), Fig.7.c)) clearly show that resolution of this method is good enough for the profile measurements of the surface with average roughness (half width at half maximum) of the order of 1 nm. Note here that we consider height resolution as a rms (root mean square) of measured values of height.

Unfortunately, instrumental function of interferometer introduces phase distortions which are not allowed resolving the isolated atomic steps which are situated on the analyzed surface.
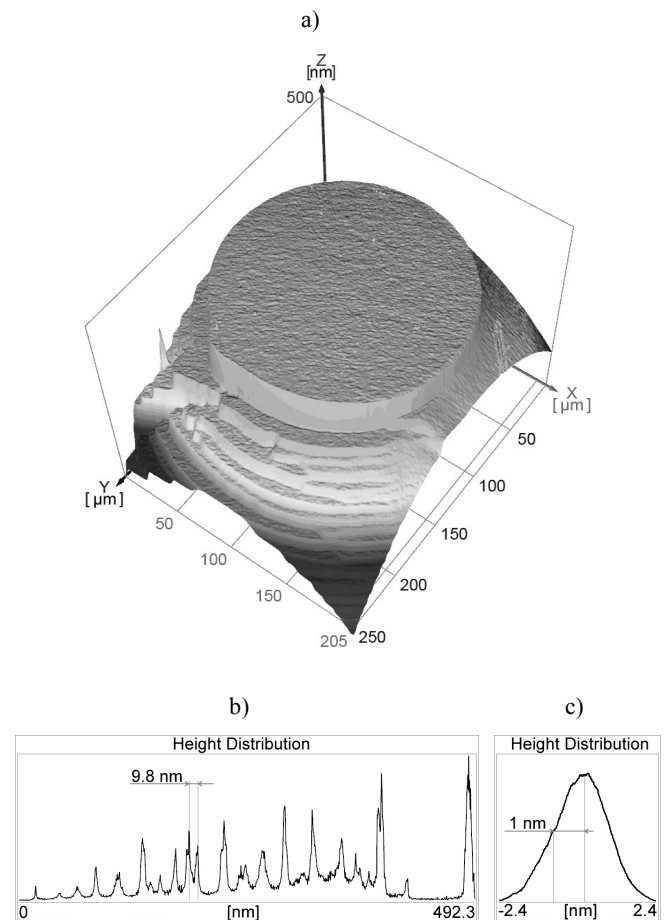
Fig.7. The reconstructed 3D model of surface a) and height distribution for the whole area b) and central region c).

To eliminate the influence of instrumental function the differential measurement of surface nanorelief was proposed. Two measurements of the same sample situated in the different positions in the plane *XY* were carried out: first is the initial position, the second is a position shifted by about 15 µm. Further, the measurement results which were obtained for two positions of sample were subtracted one from another. The result of differential measurements of surface nanorelief containing monoatomic steps is shown in Fig.8. Thus, the differential measurement of surface nanorelief performed by nanoprofiler MNP-1 allowed us to register the structure of monoatomic steps on the sample surface.
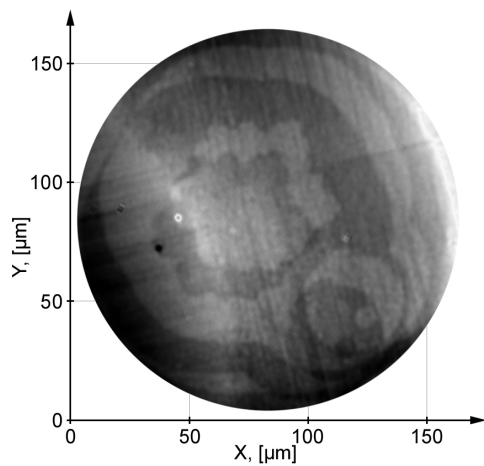
Fig.8. Results of differential measurements of surface nanorelief with monoatomic steps.

5. PICOMETER HEIGHT PROFILOMETRY BY USING ATOMICALLY SMOOTH MIRROR

In order to increase the height resolution of nanoprofiler MNP-1, special silicon sample containing wide and extremely smooth surface area was designed by ISP SB RAS. We proposed to place this surface in the reference arm of the interferometer and use it as a reference mirror.
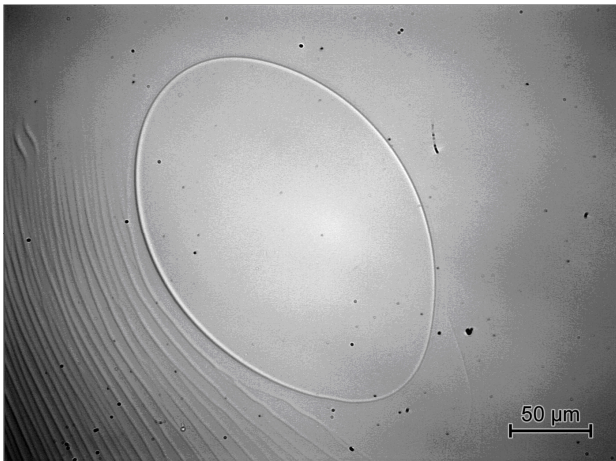
Fig.9. Optical image of the reference mirror with atomically-smooth region of silicon.

This sample contains the surface region (atomically-smooth singular terrace) with an average roughness R_a below 0.03 nm [8]. Microphotograph of this reference mirror obtained in MNP-1 is shown in Fig.9. Atomically smooth region of the surface in the form of ellipse with sizes 200 µm × 160 µm is clearly seen at the center of image.

After installation of atomically smooth surface in the reference interferometer arm, the measurement of silicon sample with relief structure height of one interatomic distance was performed again.
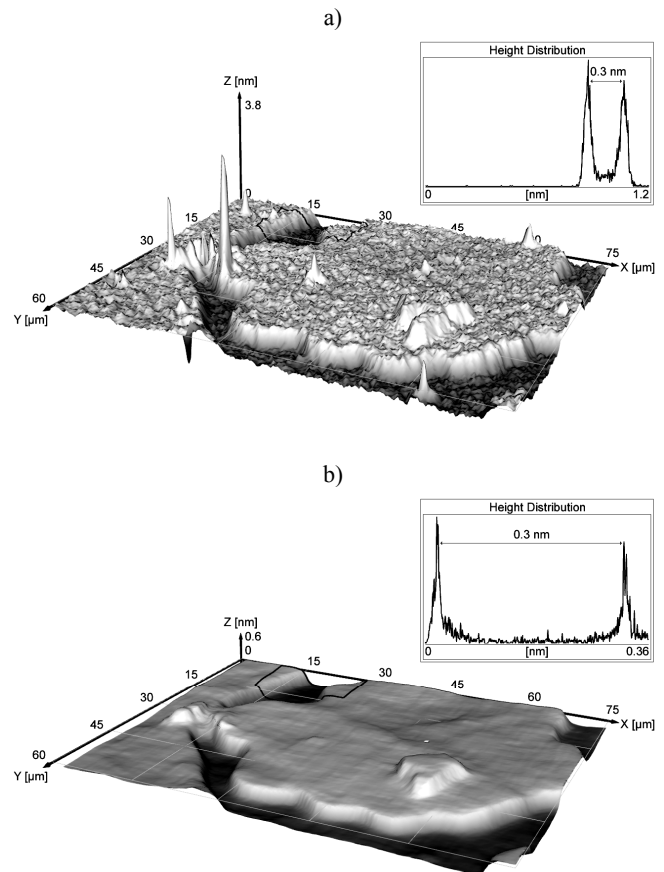
Fig.10. 3D surface relief reconstruction of Si (111) sample without a) and after spatial filtering b) with plot of height distributions for selected areas (insets).

Fig.10. represents the measurement results of the same sample surface area as in Fig.6., Fig.7. (central region), and Fig.8. which were obtained by the new reference mirror. The measurement results of the sample without filtering are shown in Fig.10.a).

In the case of preliminary knowledge of object morphology, the application of various filters for resolution increase will be effective. In particular, under the measurements of monoatomic steps one can use averaging and(or) median filtering with window width about half of characteristic size of steps. The results of measurements of monoatomic step with size about 20 µm are shown in Fig.10.a). In this case the filter with size of 10 µm was used (Fig.10.b)). Thus, the application of such filter is correct and

allows us to fulfill the measurement of monoatomic step with higher accuracy.

It was shown that even without filtration of measured surface relief the use of atomic smooth mirror allows us to drastically increase the height resolution and measure the height of monoatomic steps.

The measurements of step height and measurements ambiguity were carried out by standard method using the histogram of height distribution. Height of steps (Fig.10.a), Fig.10.b)) was calculated as a distance between graph extrema, and the ambiguity of height definition of steps was estimated by standard deviation. The height distributions shown at insets of Fig.10.a), Fig.10.b) allow us to estimate height resolution of this method as 30 and 5 pm for case without filtering and after applying spatial filter, respectively.

6. CONCLUSION

The experimental results carried out by MNP-1 at the surface relief measurement of silicon sample with monoatomic layers structure are shown. Due to differential measurements, the nanoprofiler MNP-1 has been able to detect monoatomic structure.

Technical parameters of MNP-1 were following:

Objectives	20×;
CCD-camera	frame rate 30 fps; matrix 1392 × 1040 pixels; pixel size 6.45 μm; s/n ratio 60 dB.;
Measurement range	up to 20 μm;
Height resolution	not worse than 0.1 nm;
Lateral resolution	0.79 μm (for 630 nm);
Measurement area	0.45 mm × 0.33 mm;
Measurement speed	20 μm to 10 seconds.

For improvement height resolution of MNP-1, special silicon sample (designed at ISP SB RAS) containing wide and extremely smooth surface area (atomically smooth mirror) was proposed to use as a reference mirror in the interferometer.

The obtained results show that using an atomically smooth surface as the reference mirror of the interferometer and the method of partial correlogram scanning drastically improve the height resolution of nanoprofiler below 30 pm and allow one to visualize monatomic steps on silicon surface.

It is essential that preliminary knowledge of measurement object structure allowed us to use the processing of the measurement result and to obtain resolution by height 5 picometers.

As an extension of the work it is proposed to carry out experiments to measure surface relief of sample with monoatomic structures by means of interferometer which contains both atomic smooth reference mirror and stable laser radiation source.

REFERENCES

[1] Guilemany, J.M., Miguel, J.M., Armada, S., Vizcaino, S., Climent, F. (2001). Use of scanning white light interferometry in the characterization of wear mechanisms in thermal-sprayed coatings. *Materials Characterization*, 47 (3-4), 307-314.

[2] De Groot, P., Biegen, J., Clark, J., Lega, X.C., Grigg, D. (2002). Optical interferometry for measurement of the geometric dimensions of industrial parts. *Applied Optics*, 41 (19), 3853-3860.

[3] De Groot, P. (2011). Coherence scanning interferometry. In *Optical Measurement of Surface Topography*. Springer, 187-208.

[4] Niehues, J., Lehmann, P., Xie, W. (2012). Low coherent Linnik interferometer optimized for use in nano-measuring machines. *Measurement Science and Technology*, 23 (12), 125002.

[5] Windecker, R., Fleischer, M., Körner, K., Tiziani, H.J. (2001). Testing micro devices with fringe projection and white-light interferometry. *Optics and Lasers in Engineering*, 36 (2), 141-154.

[6] Hariharan, P., Malakara, D. (1995). *Selected Papers on Interference, Interferometry, and Interferometric Metrology*. SPIE Optical Engineering Press.

[7] Creath, K., Wyant, J.C. (1990). Absolute measurement of surface roughness. *Applied Optics*, 29 (26), 3823-3827.

[8] Sitnikov, S.V., Kosolobov, S.S., Shcheglov, D.V., Latyshev, A.V. (2011). *Method of forming flat smooth surface of solid material*. Patent RU 2453874.

[9] Sysoev, E.V. (2007). White-light interferometer with partial correlogram scanning. *Optoelectronics, Instrumentation and Data Processing*, 43 (1), 83-89.

[10] Sysoev, E.V., Vykhristuk, I.A., Kulikov, R.V., Potashnikov, A.K., Razum, V.A., Stepnov, L.M. (2010). Interference microscope-profilometer. *Optoelectronics, Instrumentation and Data Processing*, 46 (2), 198-205.

[11] Rosenberg, G.V. (1953). Interferencionnaya mikroskopiya. *Uspehi fizicheskih nauk*, L (2), 279-281. (in Russian)

[12] Dubois, A., Selb, J., Vabre, L., Boccara, A.-C. (2000). Phase measurement with wide-apperture interferometers. *Applied Optics*, 39 (14), 2326-2331.

Performance Degradation Assessment of Rolling Element Bearings using Improved Fuzzy Entropy

Keheng Zhu[1], Xiaohui Jiang[1], Liang Chen[2], Haolin Li[1]

[1]*School of Mechanical Engineering, University of Shanghai for Science and Technology, Jungong Road, Shanghai 200093, PR China, khzhdl@gmail.com*
[2]*School of Energy and Power Engineering, Dalian University of Technology, Linggong Road, Dalian 116023, PR China*

Rolling element bearings are an important unit in the rotating machines, and their performance degradation assessment is the basis of condition-based maintenance. Targeting the non-linear dynamic characteristics of faulty signals of rolling element bearings, a bearing performance degradation assessment approach based on improved fuzzy entropy (FuzzyEn) is proposed in this paper. FuzzyEn has less dependence on data length and achieves more freedom of parameter selection and more robustness to noise. However, it neglects the global trend of the signal when calculating similarity degree of two vectors, and thus cannot reflect the running state of the rolling element bearings accurately. Based on this consideration, the algorithm of FuzzyEn is improved in this paper and the improved FuzzyEn is utilized as an indicator for bearing performance degradation evaluation. The vibration data from run-to-failure test of rolling element bearings are used to validate the proposed method. The experimental results demonstrate that, compared with the traditional kurtosis and root mean square, the proposed method can detect the incipient fault in advance and can reflect the whole performance degradation process more clearly.

Keywords: Performance degradation assessment, improved fuzzy entropy, rolling element bearing.

1. INTRODUCTION

Machinery condition monitoring has received considerable attention for many years because a reliable condition monitoring system can significantly reduce the huge cost due to the unplanned downtime [1]-[2]. Rolling element bearings are the most widely used component in the rotating machines, and they are also one of the most easily damaged mechanical parts. The running state of bearing influences the reliable operation of the whole machine. Therefore, the bearing condition monitoring is of great importance to keep machines running reliably and reduce economical loss. Among various condition monitoring methods, the most suitable and effective one is vibration analysis because vibration signals of rolling element bearings include abundant fault information [3]-[4].

Diagnosis and prognosis are the two important aspects of condition-based maintenance. Performance degradation assessment is the base of prognosis which is much more efficient than fault diagnosis to achieve zero-downtime performance [1]. It requires reflecting the comprehensive performance degradation degree based on the extracted features and focuses on the vibration trend over a whole lifetime while traditional fault diagnosis only needs to be capable of identifying different types of faults. To date, many researches on the performance degradation assessment of rolling element bearings have been carried out, most of which are based on the intelligent assessment approaches, such as self-organizing map (SOM) [5]-[6], hidden Markov model (HMM) [7], support vector data description (SVDD) [8]-[10], Gaussian mixture model (GMM) [11] and logistic regression (LR) [12]. However, these proposed intelligent assessment models may all exhibit their own limitations [13]-[14]. For example, ANN-based model operates as a "black box" without documentation of qualitative information of the model and requires large amount of training data [13], HMM-based model needs assumptions which are unpractical in the real applications [14] and Gaussian process-based model is only suitable for Gaussian likelihood and has a heavy computation burden [13].

On the other hand, designing proper indicators without intelligent models has not received enough attention in previous studies, and some existing statistical indicators in the time domain have their own advantages and limitations as well. For example, the extensively used root mean square (RMS) can steadily grow with the defect evolution of the bearing, but it is insensitive to the early faults. On the contrary, kurtosis and crest factor are sensitive enough to impulse defect at the incipient stage but reduce to normal-like levels as the damage grows [7]. Hence, exploring new effective indicators, which can reflect the comprehensive degeneration process of rolling element bearings, is valuable work [15].

As it is known, vibration signals of a bearing, especially when fault occurs, will present non-linear characteristics due to the non-linear factors such as stiffness, friction and clearance [16]. For this reason, the traditional time and frequency domain signal analysis methods based on the linear systems, even the advanced signal processing methods such as wavelet transform, are usually hard to make an accurate assessment of the bearing running states. With the development of nonlinear dynamics theory, various nonlinear analysis approaches have offered a good alternative to identify and predict the complicated non-linear dynamic behavior of bearings, among which entropy-based parameters, such as appropriate entropy (ApEn), sample entropy (SampEn), multi-scale entropy (MSE), and hierarchical entropy (HE) have been researched and introduced to the field of bearing fault diagnosis [17]-[19]. Due to the bias caused by self-matching, ApEn depends heavily on the data length and its estimated value is uniformly lower than the expected one, especially as short data concerned, and lacks relative coherence as well [20]. In order to overcome the shortcomings of ApEn, Richman and Moorman [21] developed another related measure of signal complexity, viz. SampEn, which is less dependent on dataset length and has better relative consistency. However, the definitions of similarity between vectors in SampEn and ApEn are both based on Heaviside function, whose boundary is discontinuous and rigid. Due to the inherent flaws of Heaviside function, there still exist problems in the validity of the entropy definition. In order to address the problems, Chen et al. [22] presented recently a measure of complexity named fuzzy entropy (FuzzyEn) by improving the original SampEn. In comparison with SampEn, FuzzyEn uses fuzzy membership functions to replace Heaviside function for making a soft and continuous boundary, which makes FuzzyEn well defined at small parameters and enables it to change continuously. Nevertheless, the fuzzy function used in FuzzyEn by Chen et al. was deemed to lack clear physical meanings [23]. Therefore, Zheng et al. [24] defined a new fuzzy function and used the optimized one to measure the complexity of vibration signals of rolling element bearings. However, the limitation of FuzzyEn is that it neglects the global characteristics of the signal and thus may produce inaccurate results [25].

As a bearing runs from a normal condition to a faulty one, the vibration signals will present different characteristics with the bearing state varying. Moreover, the fault severity and growth of rolling element bearings have been proved by the previous researches that they are associated with the changes of the entropy values (such as ApEn, MSE and HE), which makes them attractive tools for monitoring system dynamics [17]-[19]. In this study, inspired by these existing researches, we modified the algorithm of FuzzyEn to relieve the aforementioned limitation and used the improved FuzzyEn as an indicator for bearing performance degradation. Considering the fact that the global characteristics and global trends of bearing vibration signals may change as the bearing degenerates gradually, the improved FuzzyEn should be more suitable to reflect the bearing degradation process over its whole lifetime. The effectiveness of the modified FuzzyEn for bearing performance degradation evaluation is then investigated through experimental data.

The paper is organized as follows. Section 2 is dedicated to the improved FuzzyEn method. The vibration data from a laboratory test-to-failure test are employed to validate the effectiveness of the proposed method in section 3. In section 4, conclusions from this research are presented.

2. THE IMPROVED FUZZY ENTROPY METHOD

2.1. Fuzzy entropy

SampEn is a refinement of ApEn and is free of bias caused by self-matching. Details on the calculation of SampEn can be found in previous researches [21]-[23]. The computation of the vectors' similarity in SampEn is defined based on Heaviside function, which is discontinuous and makes a binary decision on the similarity between vectors according to their distance. However, in the real physical world, it is hard to decide whether a pattern belongs to a given class because boundaries between classes may be ambiguous. Hence, FuzzyEn is developed to overcome the drawback of SampEn by replacing the Heaviside function with a continuous Gaussian type function, which is utilized to measure the similarity degree instead of a binary decision.

The FuzzyEn algorithm can be described as follows [22]:
1. For a time series of N points $\{u(i):1{\leq}i{\leq}N\}$, form the m-length vectors,

$$X_i^m = \{u(i),u(i+1),...,u(i+m-1)\} - u_0(i) \tag{1}$$

where $1{\leq}i{\leq}N - m + 1$ and X_i^m denotes m consecutive u values, commencing with the ith point and generalized by removing their baseline

$$u_0(i) = m^{-1}\sum_{j=0}^{m-1} u(i + j) \tag{2}$$

2. The distance between X_i^m and X_j^m is defined as the maximum absolute difference of the corresponding scalar components

$$\begin{aligned}
d_{ij}^m &= d\left[X_i^m - X_j^m\right] \\
&= \max_{k\in[0,m-1]}\left|(u(i + k) - u_0(i)) - (u(j + k) - u_0(j))\right|
\end{aligned} \tag{3}$$

3. The similarity degree D_{ij}^m of X_i^m to X_j^m is calculated with a fuzzy function

$$D_{ij}^m = \mu(d_{ij}^m, r) \tag{4}$$

4. For each X_i^m, average all the similarity degrees of its neighboring vectors X_j^m, then designate

$$\varphi_i^m(r) = (N - m - 1)^{-1} \sum_{j=1, j \neq i}^{N-m} D_{ij}^m \qquad (5)$$

5. Define the function $\varphi^m(r)$ as

$$\varphi^m(r) = (N - m)^{-1} \sum_{i=1}^{N-m} \varphi_i^m(r) \qquad (6)$$

6. Similarly, for the dimension $m+1$, repeat the previous procedures and the $\varphi^{m+1}(r)$ is defined as

$$\varphi^{m+1}(r) = (N - m)^{-1} \sum_{i=1}^{N-m} \varphi_i^{m+1}(r) \qquad (7)$$

7. FuzzyEn of the time series is then denoted as

$$FuzzyEn(m, r) = \lim_{N \to \infty} [\ln \varphi^m(r) - \ln \varphi^{m+1}(r)] \qquad (8)$$

8. Finally, for a finite number of data points N, its estimation can be estimated by the statistic

$$FuzzyEn(m, r, N) = \ln \varphi^m(r) - \ln \varphi^{m+1}(r) \qquad (9)$$

Originally, the exponential function was adopted to fuzzily measure the similarity between vectors by Chen et al. [22], which was defined as

$$\mu(d_{ij}^m, r, n) = e^{-(d_{ij}^m / r)^n} \qquad (10)$$

In order to make FuzzyEn more physically meaningful, Zheng et al. [24] designed a new membership function to substitute the original one as

$$\mu(d_{ij}^m, r, n) = e^{-\ln 2(d_{ij}^m / r)^n} \qquad (11)$$

In this paper, equation (11) is applied to compute FuzzyEn of bearing vibration signals, and an assessment of its performance is made.

2.2. The improved fuzzy entropy

A change in the definition of the aforementioned FuzzyEn is the formation of the vector X_i^m, which is generalized by

removing a baseline defined by (2). However, this implementation of removing the baseline focuses only on the local characteristics of the signal and neglects its global trend [25]. As for the bearing vibration signals, their global characteristics may vary with the running states of bearings deteriorating gradually. Therefore, it may be not enough to reflect the bearing performance degradation process effectively by using the original FuzzyEn. Based on this consideration, we modified (1) as

$$X_i^m = \{u(i), u(i+1), \dots, u(i+m-1)\} \qquad (12)$$

Which means the local mean is removed. In this study, in order to reflect the bearing degradation states more accurately, equation (12) was utilized to calculate the values of FuzzyEn. The modified FuzzyEn is then employed to measure the complexity of vibration signals of rolling element bearings, and the obtained entropy value is defined as the bearing degradation indicator. Finally, the performance of the improved FuzzyEn for bearing degradation evaluation was assessed with experimental data.

2.3. Parameters selection

There are four parameters that need to be selected for each calculation of FuzzyEn, which is m, r, N, and n, respectively. The parameter m is the length of sequences to be compared. Typically, larger m allows more detailed reconstruction of the dynamic process [22]. However, a too large m value needs a very large N (10^m-30^m), which is unfavorable in many real applications. Generally, m is chosen as 2, and N is selected as 2048 in this paper. The width and gradient of the boundary of the exponential function are determined by the parameters r and n, respectively, viz. the fuzzy similarity boundary. A too narrow boundary will result in noticeable influence from noise while a too broad one will lead to the loss of information. According to the previous studies [18]-[19], r = 0.1-0.25SD (standard deviation of the original data) and n should be small integers. To seek a balance between noise robustness and information loss, r = 0.2SD is assigned, and n = 2 is selected.

3. EXPERIMENTAL VALIDATION

3.1. Experimental data

In order to investigate the effectiveness of the modified FuzzyEn for the rolling element bearing performance degradation assessment, vibration signals from run-to-failure experiments are analyzed. The bearing vibration data is from the prognostic data repository contributed by the Center on Intelligent Maintenance Systems (IMS), University of Cincinnati [26].

The bearing test rig is shown in Fig.1., which consists of one shaft, four test bearings, an AC motor and rub belts. Four Rexnord ZA-2115 double row bearings were installed on one shaft. The shaft was driven by the AC motor and coupled by rub belts. The rotational speed was kept constantly at 2000 rpm and a radial load of 6000 lbs was applied to the shaft and bearing through a spring mechanism.

The lubrication of all the bearings was provided by an oil circulation system and the flow and temperature of the lubricant was regulated by the system. A magnetic plug was installed in the oil feedback pipe to collects debris from the oil as evidence of bearing degradation. When the accumulated debris adhering to the magnetic plug exceeded a certain level, an electrical switch closed and the test stopped. A PCB 352B33 High Sensitivity Quarts ICP accelerometer was installed on each bearing housing to collect the vibration signals. The vibration data was collected every 10 min at a sampling frequency of 20 kHz and the data length was 20480 points.
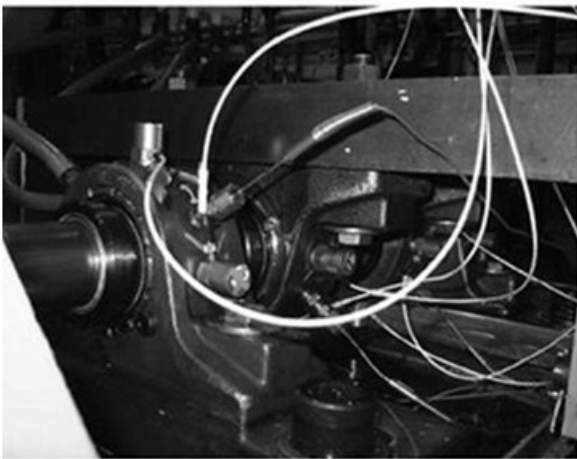
Fig.1. Bearing test rig.
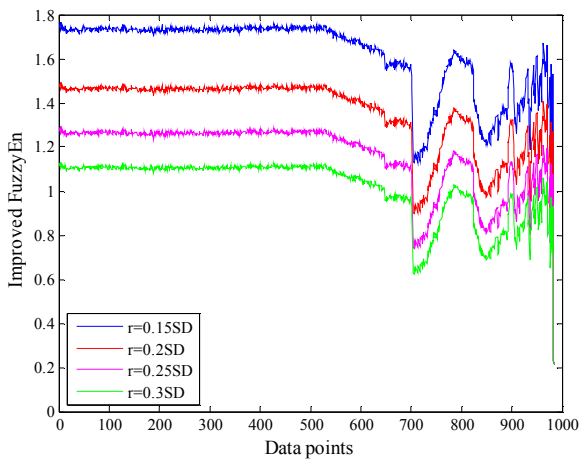
Fig.2. Effect of parameter r on the improved FuzzyEn values.

3.2. Effects of parameter selection

As mentioned above, the calculation of FuzzyEn depends less on dataset length N and a too large m value requires a very large N, which is unpractical in many real applications. In the present study, based on the aforementioned experimental signals, the effects of parameters r and n on the computation of the improved FuzzyEn have been investigated. The effect of different r ($n = 2$) on the FuzzyEn values is shown in Fig.2., from which it can be seen that the

larger the r is, the smaller the entropy value is. Although they vary with r increasing, the FuzzyEn values keep the same variation trend as the r changed. The effect of different n ($r = 0.2$SD) on the FuzzyEn values is given in Fig.3. From Fig.3., we can see that the larger the n is, the larger the entropy value is. Nevertheless, similarly to r, the FuzzyEn values keep the same variation trend with n changing. From Fig.2. and Fig.3., it can be observed that the changes of parameter r and n have little influence on the bearing performance degradation assessment. Considering all the above factors, in this paper, m is fixed as 2, and N is chosen as 2048 while $r = 0.2$SD is selected, and $n = 2$ is assigned.
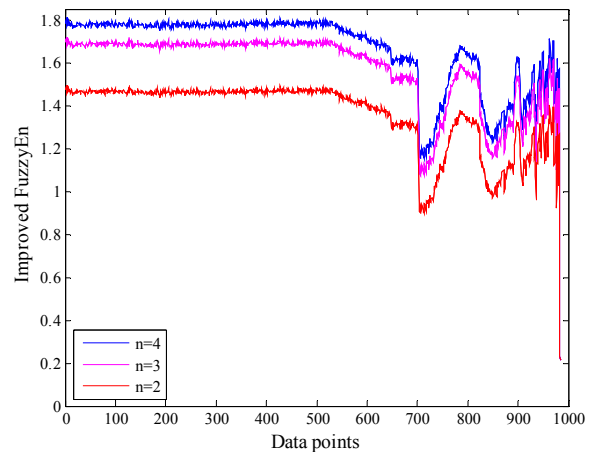
Fig.3. Effect of parameter n on the improved FuzzyEn values.

3.3. Results and analysis

The bearing vibration signals from test 2 are employed for analysis. At the end of this experiment, an outer race defect was found in bearing 1. There are 984 data files being collected in this experiment. The FuzzyEn values of the bearing vibration data are then calculated and used as the bearing degradation indicator. In order to avoid the influence of random factors on the computation of FuzzyEn values, each data file is separated into 10 segments (each segment length is 2048), and the mean value of FuzzyEn of these 10 segments can be obtained.

The variations of SampEn, FuzzyEn and improved FuzzyEn with time are shown in Fig.4., respectively. It can be seen that the entropy values of SampEn and improved FuzzyEn show a similar trend while the values of original FuzzyEn present a different way. The variance trends of SampEn and improved FuzzyEn demonstrate that the entropy values keep stable for a long-time period when bearing is running under normal condition and begin to decrease as early fault occurs, which means that the vibration signals of healthy bearing are more complex than those of faulty bearing. According to the literature [24], this can be explained by the fact that the vibration signals under normal condition have lower self-similarity because of its randomness and irregularity, and the self-similarity will increase as the fault appears. As for the original FuzzyEn, some of its values in bearing degradation area (nearby the

final failure) are much larger than these under healthy condition, which will result in mistaken decision. This may be due to the fact that it subtracts the local mean during the algorithm implementation and thus neglects the global trend of bearing vibration signal. In addition, compared with SampEn, there exists a smaller range of fluctuation in the improved FuzzyEn values during the bearing's whole lifetime, which means improved FuzzyEn presents a better statistical stability than SampEn. This is because a fuzzy membership function is adopted in improved FuzzyEn to define the decision rule for vector similarity while a piecewise function is used in SampEn. Therefore, the improved FuzzyEn is most suitable for bearing degradation assessment.
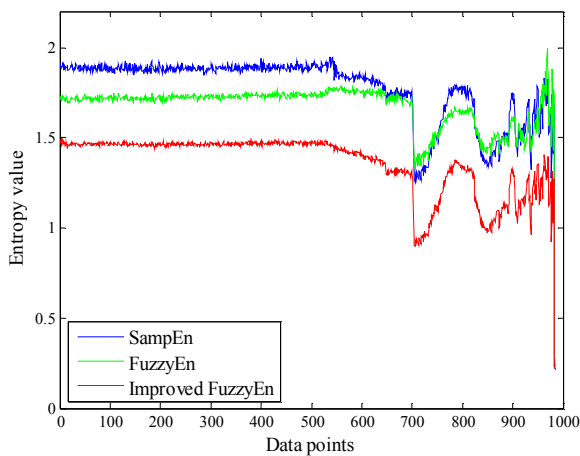
Fig.4. Comparison of SampEn, FuzzyEn and improved FuzzyEn over bearing's whole lifetime.

Fig.5. The variation of SampEn values with time.

In order to further show the advantage of the improved FuzzyEn over SampEn, the corresponding curves with local enlargement are illustrated in Fig.5. and Fig.6., respectively. From Fig.5. and Fig.6., it can be observed that the SampEn values indicate the occurrence of initial degradation at the 546th data point while the improved FuzzyEn values start to decrease at the 533th data point, which means that the

improved FuzzyEn can detect the incipient degradation 13 data points in advance. For comparison purpose, another two degradation assessment indicators, root mean square (RMS) and the kurtosis value, are also calculated and shown in Fig.7. and Fig.8., respectively. It can be seen from Fig.7. that RMS values indicate the occurrence of degradation at the 535th data point, which is two data points behind compared with the values of improved FuzzyEn. Moreover, the increase of RMS values is less obvious than that of improved FuzzyEn. From Fig.8., it can be observed that the bearing performance degradation begins at about the 648th data point, which is more than 100 data points later than that indicated by improved FuzzyEn. In addition, the kurtosis values decrease sharply as the occurrence of final failure, which makes the prediction of bearing degradation degree impossible.

Fig.6. The variation of values of improved FuzzyEn with time.

Fig.7. The variation of RMS values with time.

According to the above analysis, the following can be observed: (1) Compared with SampEn and original FuzzyEn, the improved FuzzyEn is the most suitable for performance degradation evaluation of rolling element bearings. (2) The modified FuzzyEn values can assess the bearing

performance degradation process over their whole life time clearly and effectively. (3) In contrast with kurtosis and RMS, the modified FuzzyEn can detect the bearing initial degradation in advance, which is of great significance for the prognosis in the condition monitoring.
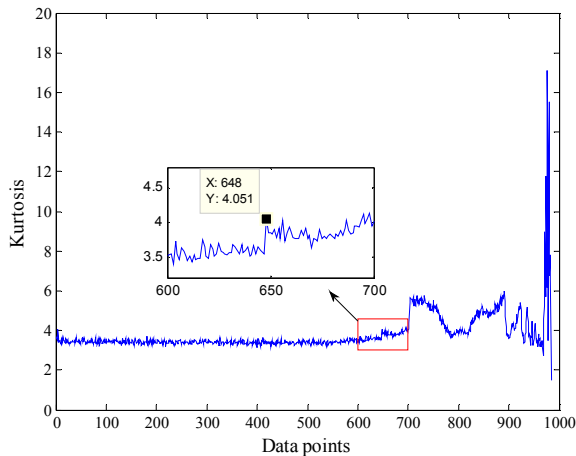
Fig.8. The variation of kurtosis values with time.

4. CONCLUSIONS

In this paper, the FuzzyEn is improved and used as an indicator for the performance degradation assessment of rolling element bearings. The run-to-failure vibrational signals are applied to verify the suitability of the improved FuzzyEn method. The experimental results demonstrate that the modified FuzzyEn can reflect the bearing degradation process effectively and has shown better performance than SampEn and original FuzzyEn. Compared with RMS, the improved FuzzyEn can indicate the initial degradation two data points in advance and presents a more obvious increase. In contrast with kurtosis, the improved FuzzyEn can detect the occurrence of degradation more than 100 data points ahead and shows a clearer and more accurate trend for bearing degradation process over its whole lifetime.

ACKNOWLEDGMENT

REFERENCES

[1] Jardine, A.K.S., Lin, D.M., Banjevic, D. (2006). A review on machinery diagnostics and prognostics implementing condition-based maintenance. *Mechanical Systems Signal Processing*, 20 (7), 1483–1510.

[2] Huang, H.F., Ouyang, H.J., Gao, H.L., Guo, L., Li, D., Wen, J. (2016). A feature extraction method for vibration signal of bearing incipient degradation. *Measurement Science Review,* 16 (3), 149-159.

[3] Tandon, N., Choudhury, A. (1999). A review of vibration and acoustic measurement methods for the detection of defects in rolling element bearings. *Tribology International*, 32 (8), 469-480.

[4] Gebraeel, N., Lawley, M., Liu, R., Parmeshwaran, V. (2004). Residual life predictions from vibration-based degradation signals: A Neural Network approach. *IEEE Transactions on Industrial Electronics*, 51 (3), 694-700.

[5] Qiu, H., Lee, J., Lin, J., Yu, G. (2003). Robust performance degradation assessment methods for enhanced rolling element bearing prognostics. *Advanced Engineering Informatics*, 17 (3), 127-140.

[6] Huang, R.Q., Xi, L.F., Li, X.L., Liu, C.R., Qiu, H., Lee, J. (2007). Residual life predictions for ball bearings based on self-organizing map and back propagation neural network methods. *Mechanical Systems Signal Processing*, 21 (1), 193–207.

[7] Ocak, H., Loparo, K.A., Discenzo, F.M. (2007). Online tracking of bearing wear using wavelet packet decomposition and probabilistic modeling: A method for bearing prognostics. *Journal of Sound Vibration*, 302 (4), 951–961.

[8] Pan, Y.N., Chen, J., Guo, L. (2009). Robust bearing performance degradation assessment method based on improved wavelet packet–support vector data description. *Mechanical Systems Signal Processing*, 23 (3), 669–681.

[9] Shen, Z.J., He, Z.J., Chen, X.F., Sun, C., Liu, Z. (2012). A monotonic degradation assessment index of rolling bearings using fuzzy support vector data description and running time. *Sensors*, 12 (8), 10109-10135.

[10] Zhu, X.R., Zhang, Y.Y., Zhu, Y.S. (2013). Bearing performance degradation assessment based on the rough support vector data description. *Mechanical Systems Signal Processing*, 34 (1), 203–217.

[11] Yu, J.B. (2011). Bearing performance degradation assessment using locality preserving projections and Gaussian mixture models. *Mechanical Systems Signal Processing*, 25 (7), 2573–2588.

[12] Caesarendra, W., Widodo, A., Thom, P.H., Yang, B.S., Setiawan, J.D. (2011). Combine probability approach and indirect data-driven method for bearing degradation prognostics. *IEEE Transactions Reliability*, 60 (1), 14-20.

[13] Kan, M.S., Tan, A.C.C., Mathew, J. (2015). A review on prognostic techniques for non-stationary and non-linear rotating systems. *Mechanical Systems Signal Processing*, 62-63, 1–20.

[14] Peng, Y., Dong, M., Zuo, M.J. (2010). Current status of machine prognostics in condition-based maintenance: A review. *International Journal of Advance Manufacturing Technology*, 50 (1), 297-313

[15] Dong, G.M., Chen, J. (2010). Study on cyclic energy indicator for degradation assessment of rolling element bearings. *Journal of Vibration and Control*, 17 (12), 1805-1816.

[16] Yang, Y., Yu, D.J., Cheng, J.S. (2006). A roller bearing fault diagnosis method based on EMD energy entropy and ANN. *Journal of Sound and Vibration*, 294 (1), 269-277.

[17] Yan, R.Q., Gao, R.X. (2007). Approximate entropy as a diagnostic tool for machine health monitoring. *Mechanical Systems Signal Processing*, 21 (2), 824-839.

[18] Zhang, L., Xiong, G.L., Liu, H.S., Zou, H., Guo, W. (2010). Bearing fault diagnosis using multi-scale entropy and adaptive neuro-fuzzy inference. *Expert Systems with Applications*, 37 (8), 6017-6085.

[19] Zhu, K.H., Song, X.G., Xue, D.X. (2014). A roller bearing fault diagnosis method based on hierarchical entropy and support vector machine with particle swarm optimization algorithm. *Measurement*, 47, 669-675.

[20] Pincus, S.M. (1991). Approximate entropy as a measure of system complexity. *Proceedings of the National Academy of Sciences*, 88 (6), 2297-2301.

[21] Richman, J.S., Moorman, J.R. (2000). Physiological time-series analysis using approximate entropy and sample entropy. *American Journal of Physiology-Heart and Circulatory Physiology*, 278 (6), H2039-H2049.

[22] Chen, W.T., Wang, Z.Z., Xie, H.B., Yu, W. (2007). Characterization of surface EMG signal based on fuzzy entropy. *IEEE Transactions on Neural Systems and Rehabilitation Engineering*, 15 (2), 266-272.

[23] Xiong, G.L., Zhang, L., Liu, H.S., Zou, H.J., Guo, W.Z. (2010). A comparative study on ApEn, SampEn and their fuzzy counterparts in a multiscale framework for feature extraction. *Journal of Zhejiang University SCIENCE A*, 11 (4), 270-279.

[24] Zheng, J.D., Cheng, J.S., Yang, Y., Luo, S. (2014). A rolling bearing fault diagnosis method based on multi-scale fuzzy entropy and variable predictive model-based class discrimination. *Mechanism and Machine Theory*, 78, 187-200.

[25] Liu, C.Y., Li, K., Zhao, L.N., Liu, F., Zheng, D., Liu, C., Liu, S. (2013). Analysis of heart rate variability using fuzzy measure entropy. *Computers in Biology and Medicine*, 43 (2), 100-108

[26] Lee, J., Qiu, H., Yu, G., Lin, J. (2007). *"Bearing Data Set", NASA Ames Prognostics Data Repository.* http://ti.arc.nasa.gov/tech/dash/pcoe/prognostic-data-repository, IMS, University of Cincinnati, Rexnord Technical Services. (Accessed 13 April 2014)

MEASUREMENT SCIENCE REVIEW

Uncertainty Modeling and Evaluation of CMM Task Oriented Measurement Based on SVCMM

Hongli Li[1, 2], Xiaohuai Chen[1], Yinbao Cheng[1], Houde Liu[2], Hanbin Wang[3], Zhenying Cheng[1], Hongtao Wang[1]

[1] *School of Instrument Science and Opto-electronics Engineering, Hefei University of Technology, Tunxi Rd 193, Hefei 230009, China, lihongli_hgd@163.com / hlli@hfut.edu.cn*
[2] *Shenzhen Engineering Laboratory of Geometry Measurement Technology, Graduate School at Shenzhen, Tsinghua University, Shenzhen 518055, China*
[3] *Fujian Metrology Institute, Fuzhou 350003, China*

Due to the variety of measurement tasks and the complexity of the errors of coordinate measuring machine (CMM), it is very difficult to reasonably evaluate the uncertainty of the measurement results of CMM. It has limited the application of CMM. Task oriented uncertainty evaluation has become a difficult problem to be solved. Taking dimension measurement as an example, this paper puts forward a practical method of uncertainty modeling and evaluation of CMM task oriented measurement (called SVCMM method). This method makes full use of the CMM acceptance or reinspection report and the Monte Carlo computer simulation method (MCM). The evaluation example is presented, and the results are evaluated by the traditional method given in GUM and the proposed method, respectively. The SVCMM method is verified to be feasible and practical. It can help CMM users to conveniently complete the measurement uncertainty evaluation through a single measurement cycle.

Keywords: CMM, uncertainty modeling, uncertainty evaluation, MCM, SVCMM.

1. INTRODUCTION

The new generation Geometrical Product Specifications (GPS) requests for providing the standard uncertainty reports in product inspection and laboratory certification [1], [2]. While in the current practical applications, as indispensable and important equipment in manufacturing and product inspection, coordinate measuring machine (CMM) usually can only give the estimate of the parameters to be measured, but cannot provide the uncertainty of the measurement results [3], [4]. For the CMM users, it is difficult to complete uncertainty modeling and evaluation of CMM task oriented measurement.

The evaluation method of the sensitivity coefficient analysis and square-sum-root synthesis has been given out in the Guide to the Expression of Uncertainty in Measurement (GUM) [5], which is called GUM method in this paper for convenient expression. Although it has been widely recognized in the industry, it is usually difficult to implement in practice.

It is difficult to establish the measurement models because the CMM measurement tasks are complex and diverse. Especially for the complex or non-linear measurement model, it is very difficult to calculate the transfer coefficient and investigate the correlation between the inputs based on the GUM method, the evaluation staff needs professional knowledge about uncertainty evaluation, and extensive assessment experience [6], [7]. However, it is a practical method to evaluate uncertainty based on statistics by computer simulation [8], [9]. Evaluating measurement uncertainty by computer simulation has application prospect [10], [11], [12], [13], [14].

Taking dimension measurement as an example, this paper presents a practical method for uncertainty modeling and evaluation of CMM task oriented measurement, and also gives an evaluation example.

In this method, the measurement uncertainty analysis model is established based on measurement system analysis, and it is easy to understand and expand. Moreover, the method makes full use of the CMM acceptance or reinspection report as well as expert experience as constraint condition, and flexibly uses the Monte Carlo computer simulation (MCM) to evaluate measurement uncertainty. It is a simplified virtual coordinate measuring machine, which is abbreviated to SVCMM in this paper. The validity and practicability of this method can be demonstrated by the evaluation example.

The CMM users only need to complete a single measurement process and can realize the uncertainty evaluation of CMM task oriented measurement conveniently and effectively based on the SVCMM method.

2. MEASUREMENT UNCERTAINTY MODELING

For the dimensional measurement tasks of CMM, a general measurement model can be expressed as a function related to the coordinates of sampling points.

$$Y = g\left(x, y, z, a_1, a_2, \ldots, a_n\right) \qquad (1)$$

Where, Y is the result calculated by the measurement model, x, y, z are the measurement point coordinates, a_i is the variable parameter.

In the actual measurement process, there are many factors that will affect the measurement results. The main sources of measurement uncertainty include the CMM indication error, measurement repeatability, measurement reproducibility, workpieces inconsistence, temperature variation, and measurement speed. The main uncertainty sources are relatively independent. Among them, the temperature variation will not only bring the uncertainty of temperature compensation, but also change the thermal expansion coefficient of the measured workpiece and the thermal expansion coefficient of CMM grating ruler. For the contact measurement, the influence of workpieces inconsistence is mainly manifested as that the workpiece shape deviation or geometric deviation will affect the measurement results. The measurement speed will affect the measuring force. If the CMM works in automatic measurement mode with low speed, the probing speed of the probe is about 2 mm/sec, and the influence of measurement speed can be neglected [15].

For realizing computer automatic evaluation of measurement uncertainty, considering the influence of the main uncertainty sources, the general uncertainty analysis model of CMM oriented dimension measurement can be expressed as the following formula based on the MCM idea.

$$y = Y + \delta_E + \delta_{RP} + \delta_{RD} + \delta_T + \delta_{OBJ} + \delta_V \qquad (2)$$

Where, y is the synthetic measurement result, δ_E is the influence of CMM indication error on the measurement result, δ_{RP} is the influence of measurement repeatability on the measurement result, δ_{RD} is the influence of measurement reproducibility on the measurement result, δ_T is the influence of temperature change on the measurement result, δ_{OBJ} is the influence of measured workpieces inconsistence on the measurement result, and δ_V is the influence of measurement speed on the measurement result.

Obviously, due to different measurement personnel, there is a great deal of subjectivity in the acquisition of Y and δ_{RP}, which will directly affect the evaluation result.

Therefore, the following alternative model is proposed.

$$y = Y' + \delta_E + \delta_{RD} + \delta_T + \delta_{OBJ} \qquad (3)$$

In the formula, Y' is the average of the calculation results obtained by substituting a large number of computer simulation samples into the measurement model. The simulation samples are obtained by MCM computer simulation. They are based on one actual measurement sample, taking the maximum permissible probe error of CMM, MPE_P, as the constraint condition, and combining it with the direction cosine of the actual measuring point. Thus, Y' contains the effect of measurement repeatability, and it can reflect the randomness of detection more realistically. Moreover, the actual measurement process is carried out in the automatic low-speed measurement mode of the CMM, and the influence of the measurement speed on the measurement results can be ignored. The large sample point sets obtained by MCM simulation are based on the actual measurement sample, so the influence of measurement speed on the measurement results can also be ignored.

3. EVALUATION PROCESS OF MEASUREMENT UNCERTAINTY

Taking CMM dimensional measurement as an example, the schematic diagram of the measurement evaluation process of the proposed SVCMM method is shown in Fig.1., and the specific evaluation flow chart is shown in Fig.2.
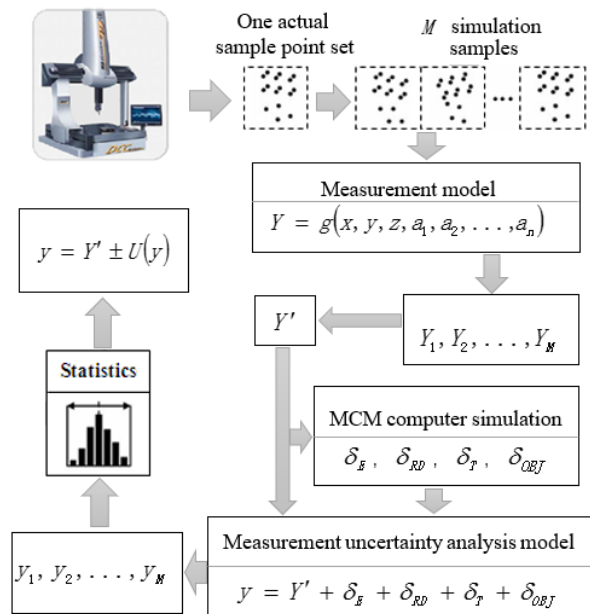
Fig.1. The schematic diagram of the SVCMM evaluation process for CMM dimensional measurement task.

As shown in Fig.2., the steps marked with "*" reflect the difference between the SVCMM evaluation and the traditional MCM evaluation.

In the traditional MCM evaluation, the single measurement result or the average value of multiple repeated measurements is used as the best estimate, and taken into the uncertainty model for synthesis. While in the SVCMM evaluation process, the actual sample points obtained in one measurement cycle are taken as the basis. According to the acceptance or reinspection report of CMM, the MCM computer simulation is used to fully reflect the

probe randomness. A large number of simulation samples are obtained and taken into the measurement model. The average of the calculated results is taken as the best estimate and used to participate in the uncertainty synthesis.

It is visible that the SVCMM evaluation method can not only reflect the impact of detection randomness on the uncertainty evaluation results more fully, but also help the CMM users to obtain reasonable uncertainty evaluation results through one measurement cycle.
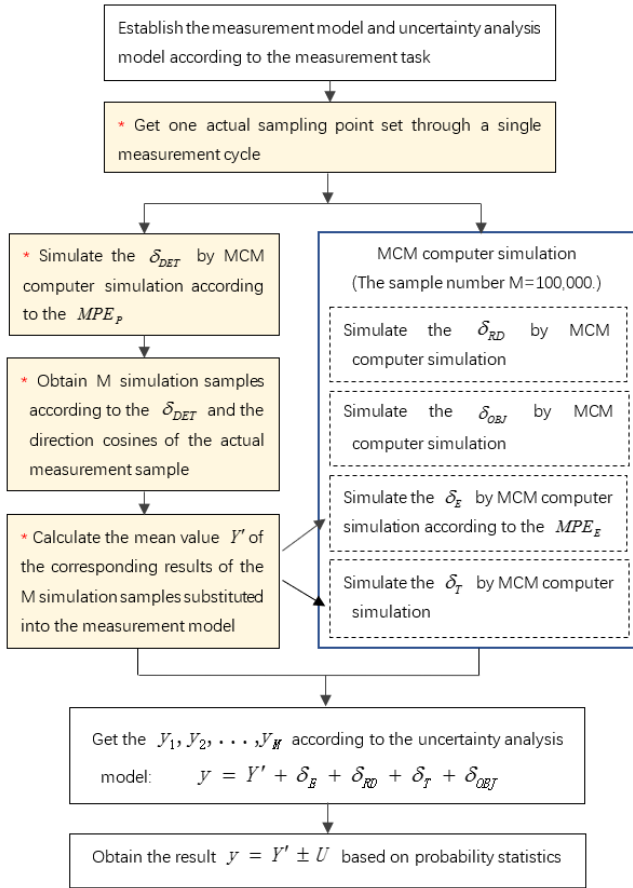
Fig.2. The SVCMM evaluation procedure of measurement uncertainty for CMM dimensional measurement task.

In order to guarantee the reliability of the uncertainty estimation, it is assumed that the effects of each error are uniformly distributed. The meaning and distribution characteristics of the variables in MCM simulation are shown in Table 1.

In Table 1., MPE_E and MPE_P are respectively the maximum permissible indication error and the maximum permissible probe error of CMM, which are provided in the acceptance or reinspection report of CMM. α_W and $\Delta\alpha_W$ are the thermal expansion coefficient of workpiece and the half width of its change, respectively. α_M and $\Delta\alpha_M$ are the thermal expansion coefficient of CMM grating ruler and the half width of its change, respectively. ΔT is the half width of the actual measurement temperature change from the

standard $20\,℃$. a_{RD} is the maximum effect of the measurement reproducibility according to the experience; a_{OBJ} is the maximum shape deviation obtained by experience or calibration measurement.

Table 1. The meaning and distribution characteristics of the variables in MCM simulation.

symbol	Meaning	Distribution characteristics
δ_{DET}	the influence of probe detection error	$U(-MPE_P, MPE_P)$
δ_E	the influence of CMM indication error	$U(-MPE_E, MPE_E)$
α'_W	the thermal expansion coefficient of workpiece	$U(\alpha_W - \Delta\alpha_W, \alpha_W + \Delta\alpha_W)$
α'_M	the thermal expansion coefficient of CMM grating ruler	$U(\alpha_M - \Delta\alpha_M, \alpha_M + \Delta\alpha_M)$
$\Delta T'$	the measurement temperature change from the standard $20\,℃$	$U(-\Delta T, \Delta T)$
δ_{RD}	the influence of measurement reproducibility	$U(-a_{RD}, a_{RD})$
δ_{OBJ}	the influence of measured workpieces inconsistence	$U(-a_{OBJ}, a_{OBJ})$

As shown in Fig.2., M samples of δ_{DETi} $(i = 1,2,\ldots, M)$ can be obtained using the MCM method to simulate the influence of detection error in M measurement cycles. According to the δ_{DETi} and the direction cosines of the actual sample points obtained in one measurement cycle, the influence of detection error on the measurement points can be converted to the three axis directions x, y, z. Then, the new M simulation samples can be obtained.

Assuming that one actual sample point is $P(x, y, z)$ and its direction cosines are (i, j, k), the corresponding new point $P'(x', y', z')$ can be obtained by (4), which has added the influence of CMM probe error according to δ_{DETi}.

$$\begin{bmatrix} x' \\ y' \\ z' \end{bmatrix} = \begin{bmatrix} x \\ y \\ z \end{bmatrix} + \begin{bmatrix} \delta_{DET} & 0 & 0 \\ 0 & \delta_{DET} & 0 \\ 0 & 0 & \delta_{DET} \end{bmatrix} \begin{bmatrix} i \\ j \\ k \end{bmatrix} \qquad (4)$$

When simulating δ_T, the influence of temperature change in the measurement process, it is important to notice the type of dimensional measurement. It can be expressed as (5) or (6) according to the measurement task belonging to internal or external dimension measurement.

$$\delta_T = \delta_{Tin} = Y' \cdot (\alpha'_M - \alpha'_W) \cdot \Delta T' \qquad (5)$$

$$\delta_T = \delta_{Tout} = Y' \cdot (\alpha'_W - \alpha'_M) \cdot \Delta T' \qquad (6)$$

Finally, the $y_1, y_2, \ldots, y_M$ can be obtained by synthesis according to the measurement uncertainty model, and the evaluation results of measurement uncertainty can be obtained through probability distribution and statistical analysis. The standard uncertainty $u(y)$ is the standard deviation of M samples. Arranging the $y_1, y_2, \ldots, y_M$ in ascending order, if given P as the contain probability, the confidence interval of the measurement results can be estimated for $\left[y_{(1-P)M/2}, y_{(1+P)M/2} \right]$ When the interval is symmetric, the expanded uncertainty and coverage factor can be determined as:

$$U(y) = \left[y_{(1+P)M/2} - y_{(1-P)M/2} \right] / 2,$$
$$k = U(y)/u(y) \qquad (7)$$

and the final measurement result can be expressed as

$$y = Y' \pm U(y) \qquad (8)$$

4. EVALUATION EXAMPLE

Taking the cylinder thickness measurement of automobile air conditioning compressor as an example, the proposed SVCMM method was applied to the uncertainty evaluation.

According to the drawings, the thickness value of the measured workpieces is 50 ± 0.02 mm. The surface roughness can be ignored. The α_W is $23.2 \times 10^{-6}/℃$, and the $\Delta \alpha_W$ is $1.0 \times 10^{-6}/℃$. Micro-Hite 3D DCC, the CMM of Hexagon, was taken as the measuring equipment. Its MPE_E is expressed as $\left(3.0 + 4.0 L / 1000 \right)$ μm, and the MPE_P is 3.5 μm. The α_M is $10.5 \times 10^{-6}/℃$, and the $\Delta \alpha_M$ is $1.0 \times 10^{-6}/℃$.

The least square measurement model of workpiece thickness is established such as (9), and the measurement uncertainty analysis model is as (10).

$$Y = \left| z_k - ax_k - by_k - c \right| / \sqrt{a^2 + b^2 + 1} \qquad (9)$$

$$y = Y + \delta_E + \delta_T + \delta_{RD} + \delta_{OBJ} \qquad (10)$$

The measurement process conformed to the operation specification and using conditions. CMM automatic measurement was used under the condition of low speed. The workpiece was placed on the measuring platform in a natural state. The probe head was configured with 4BY30, and the direction angle was T1A0B0. The measuring head was calibrated, and the workpiece coordinate system was established according to the drawing reference.

For the convenience of measurement, in one complete measurement cycle, four roughly symmetrical points P_i $(i = 1, 2, 3, 4)$ were taken on one measurement plane, one point P_k was taken from another relative end face of the workpiece. In addition, the biggest flatness of the workpiece datum was tested as 0.001 mm using the CMM

measurement software, and the maximum repeatability error was 0.0023 mm according to the measurement experience. The temperature change was about 20±1℃ in the measurement process. The coordinate data and direction cosines of the points P_i and P_k are shown in Table 2. and Table 3.

Table 2. The coordinate data and direction cosines of measured points P_i.

point	x	y	z	i	j	k
P_1	-73.0747	128.3511	-0.0018	0	0	1
P_2	119.4145	86.9125	-0.0028	0	0	1
P_3	76.5564	-112.1250	-0.0009	0	0	1
P_4	-78.0221	-78.8322	-0.0017	0	0	1

Table 3. The coordinate data and direction cosine of measured point P_k.

Measured x	Measured y	Measured z	i	j	k
30.5497	-46.4639	50.0106	0	0	1

The traditional GUM method, MCM method and the proposed SVCMM method are used to evaluate the uncertainty of the measurement results, respectively. The sample number of computer simulations is taken as $M = 100,000$, and the confidence probability is assumed as $P = 95\%$. The evaluation results are shown in Table 4. The comparison of the distributions and 95 % confidence interval limits of the results is shown in Fig.3. The comparison of the best estimate values and the confidence intervals of the results is shown in Fig.4.

Table 4. The results comparison of the workpiece thickness evaluated by GUM, MCM and SVCMM methods.

Method	y (mm)	$u(y)$ (mm)	k	U_{95} (mm)	The confidence interval satisfied for $P = 95\%$
GUM	50.0120	0.00240	2	0.0048	[50.0072, 50.0168]
MCM	50.0120	0.00237	1.89	0.0045	[50.0050, 50.0187]
SVCMM	50.0122	0.00237	1.89	0.0045	[50.0055, 50.0190]

It can be seen by comparison that the evaluation results of the three methods are more consistent. Judging by the accepted GUM evaluation results, it can be concluded that the SVCMM evaluation method is feasible and the evaluation results are effective.
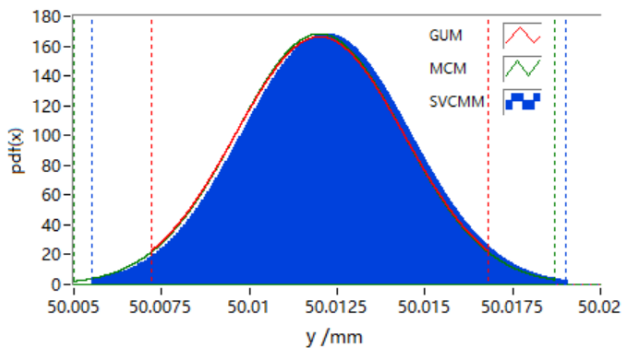
Fig.3. The distributions and 95 % confidence interval limits evaluated by GUM (red, line)，MCM (green, line) and SVCMM (blue, histogram) methods.
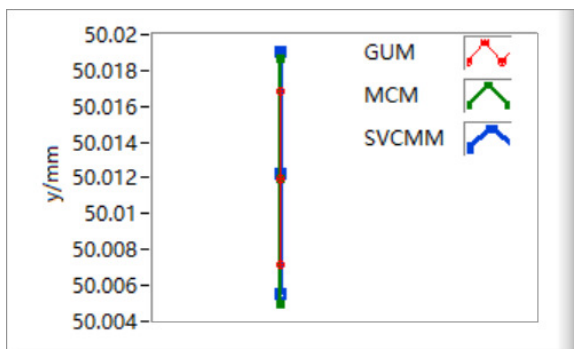
Fig.4. The best estimate values and the confidence intervals evaluated by GUM (red)，MCM (green) and SVCMM (blue) methods.

5. CONCLUSION

Taking dimension measurement as an example, this paper presents a method of uncertainty modeling and evaluation of CMM task oriented measurement.

The established uncertainty analysis model is easy to understand and easy to expand. For different geometry measurements, the error items that affect the measurement results can be changed according to the actual situation. The proposed SVCMM evaluation method is applied on the basis of the actual measurement points, so it is suitable for all dimensional measurement tasks. Especially, the SVCMM method is based on MCM computer simulation to simulate the random sampling of errors, which is more in line with the actual impact of the error. Moreover, this method is easy to carry out by computer programming, which can improve the evaluation efficiency and realize the intelligent evaluation.

The evaluation example shows that the proposed uncertainty modeling and evaluation method of CMM task oriented measurement is effective and feasible, it can help the CMM users to complete the reasonable evaluation of the measurement uncertainty through a single measurement process, and the proposed method is economical and practical. Considering the dynamic impact on measurement, further research on the measurement uncertainty evaluation

of CMM at different speeds will be carried out to improve the evaluation method.

REFERENCES

[1] International Organization for Standardization. (2003). *Measurement management systems – Requirements for measurement processes and measuring equipment.* ISO 10012:2003.

[2] International Organization for Standardization. (2011). *Geometrical Product Specifications (GPS) -- Inspection by measurement of workpieces and measuring equipment -- Part 2: Guide for the estimation of uncertainty in GPS measurement, in calibration of measuring equipment and in product verification.* ISO 14253-2:2011.

[3] Zhang, G. (1999). *Three-coordinate Measuring Machine*. China: Tianjin University Press.

[4] Chen, X., Li, H., Yang, Q., Wang, H., Cheng, Y. (2015).Task-oriented measurement uncertainty evaluation of coordinate measuring machine. *Acta Metrologica Sinica*, 36 (6), 579-583.

[5] Joint Committee for Guides in Metrology. (2008). *Evaluation of measurement data -- Guide to the expression of uncertainty in measurement*. JCGM 100:2008 (GUM 1995 with minor corrections).

[6] Štubňa, I., Šín, P., Trník, A., Vozár, L. (2014). Measuring the flexural strength of ceramics at elevated temperatures – an uncertainty analysis. *Measurement Science Review*, 14 (1), 35-40.

[7] Azpurua, M., Tremola, C., Paez, E. (2011). Comparison of the GUM and Monte Carlo methods for the uncertainty estimation in electromagnetic compatibility testing. *Progress in Electromagnetics Research B*, 34, 125-144.

[8] Joint Committee for Guides in Metrology. (2008). *Evaluation of measurement data --Supplement 1 to the "Guide to the expression of uncertainty in measurement" -- Propagation of distributions using a Monte Carlo method.* JCGM 101:2008.

[9] State Administration of Quality Supervision, Inspection and Quarantine. (2012). *Monte Carlo method for evaluation of measurement uncertainty*. JJF 1059.2-2012.

[10] Wilhelm, R.G., Hocken, R., Schwenke, H. (2001). Task specific uncertainty in coordinate measurement. *CIRP Annals*, 50 (2), 553-563.

[11] Hu, Y., Yang, Q., Sun, X. (2012). Design, implementation, and testing of advanced virtual

coordinate-measuring machines. *IEEE Transactions on Instrumentation & Measurement*, 61 (5), 1368 - 1376.

[12] Sadek, J., Gaska, A. (2012). Evaluation of coordinate measurement uncertainty with use of virtual machine model based on Monte Carlo method. *Measurement*, 45 (6), 1564-1575.

[13] Jakubiec, W., Płowucha, W., Starczak, M. (2012). Analytical estimation of coordinate measurement uncertainty. *Measurement*, 45 (10), 2299-2308.

[14] Iakovidis, S., Apostolidis, C., Samaras, T. (2015). Application of the Monte Carlo method for the estimation of uncertainty in radiofrequency field spot measurements. *Measurement Science Review*, 15 (2), 72-76.

[15] Hexagon Measurement Technology Company. (2008). *The Practical Coordinate Measuring Technology*. China: Chemical Industry Press.

Flicker Vision of Selected Light Sources

Przemysław Otomański, Grzegorz Wiczyński, Bartosz Zając

Institute of Electrical Engineering and Electronics, Poznan University of Technology, Piotrowo street, No. 3a, 60-965, Poznań, Poland

The results of the laboratory research concerning a dependence of flicker vision on voltage fluctuations are presented in the paper. The research was realized on a designed measuring stand, which included an examined light source, a voltage generator with amplitude modulation supplying the light source and a positioning system of the observer with respect to the observed surface. In this research, the following light sources were used: one incandescent lamp and four LED luminaires by different producers. The research results formulate a conclusion concerning the description of the influence of voltage fluctuations on flicker viewing for selected light sources. The research results indicate that LED luminaires are less susceptible to voltage fluctuations than incandescent bulbs and that flicker vision strongly depends on the type of LED source.

Keywords: Flicker, light source, voltage fluctuation, power quality.

1. INTRODUCTION

Voltage fluctuations influence the state of the supplied loads. Different light sources are most susceptible to fluctuation. Voltage fluctuations can cause flicker. Depending on the variability and type of the light source, flicker can be sensible or visible. With a sufficiently high intensity, flicker can be obnoxious. Nowadays, rooms are lit with incandescent lamps, discharge light sources (including the compact fluorescent lamps) and more and more frequently – LED luminaires (mostly the matrices of LED diodes). Examination of flicker vision requires experimental work using a set of representative light sources, a sufficiently large population of observers and properly set parameters of voltage fluctuation. Currently, there is no available literature to report results of such research. Nevertheless, there are reports of experimental work only for selected groups of light sources and for narrowed set of parameters of voltage fluctuation. Paper [1] presents the influence of modulation with sinusoid signal, only for 60 W of traditional bulb, on flicker severity, and the modulation range was limited to the frequency of 20 Hz. Work [2] presents the different types of fluorescent lamps with different power, for the case of modulation with voltage signal containing interharmonics of different values. Paper [3] contains the results of research concerning the dependence of flicker vision on the fluctuations of voltage containing interharmonics for a few fluorescent lamps with different types of ballasts.

This paper discusses the results of laboratory research concerning the dependence of flicker vision on voltage fluctuations. The research was conducted on a properly prepared measuring stand, which will be described further.

The following light sources were used in the research: incandescent, and LED luminaires by different manufacturers. The research was conducted for voltage fluctuations reproduced with amplitude modulation (AM) method with modulating signal frequencies in the range of (0.1–112) Hz in three sub-ranges. The result shows that the whole range of the set modulating frequencies caused flicker. There are no reports of the results of such research yet.

2. FLICKER SEVERITY CAUSED BY VOLTAGE FLUCTUATION

Measurement and evaluation of voltage variation in power network is a complex measurement problem. The values of these changes and their type (characteristic) are most frequently caused by the changes of load in power grids. One of the measures defining voltage changes is the voltage fluctuation indices. Voltage fluctuations are, according to [4], "a series of voltage changes or a continuous variation of the rms or peak value of the voltage". Such voltage variation can be characterized by simple parameters: the envelope (the shape of voltage fluctuations), magnitude and frequency (rate). A number of different indicators (P_{st} indicator [5], ΔV_{10} indicator [6]-[8], voltage fluctuation indices [9]-[10], maximum and minimum rms values [11] and others) describing voltage fluctuations are available in literature. In practice, the following values are most frequently applied: the maximal and minimal rms values of voltages, the indicators of short-time P_{st} and long-time P_{lt} flicker severity as well as the magnitude and rate of fluctuation. These are some of the most important parameters defining the power quality. Fluctuations are generated by power consumers as a result of the disturbing loads in power grids. Disturbing load is electric

equipment with repeating sudden state changes. The following loads are considered as disturbing: arc furnaces, welders, pumps, compressors, and rolling mills. In general, these are equipments with significant power in relation to short-circuit power in the point of common coupling.

Voltage fluctuations cause a number of negative influences onto loads. Different types of light sources are among the loads especially susceptible to voltage fluctuations. Flicker is the "impression of unsteadiness of visual sensation induced by a light stimulus whose luminance or spectral distribution fluctuates with time" [12]. Depending on the variability and type of light source flicker can be sensible and visible. Visual perception is a complex process, composed of three stages: the adoption of the light stimulus, its conduction and cognition. Before reaching into our eyes, light passes through the pupil. Under the influence of incident light the pupil dilates and contracts. Voltage fluctuations, and consequently flicker, may cause the motion of the eye [13] and a continuous oscillation of the pupil (hippus) [14]-[16]. This leads to human fatigue, worsening his mood, limiting their visual perception. With a sufficiently high intensity, flicker can be a reason of annoyance. The intensity of flicker to be observed depends on the type of light source, e.g. incandescent bulb, discharge lamps, LED diodes, and on their electrical-optical properties. The results of this research aim to determine the perception threshold of flicker by the participants of the experiment, depending on the voltage fluctuations for selected sources of light.

A. Standard evaluation of flicker severity caused by voltage fluctuation

As previously mentioned, flicker can cause discomfort in humans. The influence of flicker on an observer, including flicker caused by voltage supplying a light source, is a complex process [15], [17]-[25]. It depends on individual features, observer's condition, environmental conditions, properties of light source, and voltage fluctuations [26]-[28]. To evaluate the flicker severity caused by voltage fluctuations, it is necessary to apply measurement techniques used in social sciences [22], [29]. Such method of evaluating the influence of flicker on human beings is difficult to perform, and therefore, not practically applied. From the technical point of view, it is possible to measure flicker directly (with photometric sensor) in a given point [30]-[38]. This measurement has, however, two fundamental limitations. The measurement result acquired in that way describes flicker only in a certain point of lit surface. Even a slight change in the sensor location can have a significant influence on the result. Gathering representative information on flicker occurrence would require taking measurements in many appropriately selected points. Moreover, even with representative measurement results, the evaluation of flicker severity is not unequivocal. It is caused by individual sensitivity to flicker. The specified difficulties in the evaluation of the influence of flicker on human observer are the reason to search for different measurement methods.

Standard IEC 61000-4-15 [5] specifies how to evaluate the flicker caused by voltage fluctuations. The measure of severity is a pair of indicators: short-time P_{st} and long-time

P_{lt}. Current standards and legal documents defining admissible working conditions of power grids [39] refer to the P_{st}/P_{lt} indicators. To measure P_{st} indicator, a meter of flicker (flickermeter) is used. The structure of meter simulates processes occurring in the signal chain: light source - eye - brain. According to the standard specification, flickermeter determines the flicker severity caused by the fluctuations of voltage supplying a 60 W incandescent bulb. It means that for different light sources the results of measuring with flickermeter may not be representative. The reason is that flicker severity caused by the same voltage fluctuations depends on the type of light source used [38], [40]-[50]. The use of the control unit (e.g. dimmer) can also change the susceptibility of incandescent bulbs to the voltage fluctuation [51]-[52]. The long-time flicker indicator P_{lt} is calculated based on a set of values of P_{st} according to the following formula [5]

$$P_{lt} = \sqrt[3]{\frac{\sum_{i=1}^{12} P_{st_i}^3}{12}}. \tag{1}$$

Voltage variability in power grids is a complex process. The modulation of amplitude with rectangular signal is most frequently used to represent it, according to the dependence below

$$u(t) = \sqrt{2}U_c \cos(2\pi f_c t) \cdot \left[1 + \left(\frac{\Delta U}{U}\right)\frac{1}{2}\text{sign}\left\{\cos(2\pi f_m t)\right\}\right] \tag{2}$$

where: U_c – declared supply voltage, f_c – power frequency, $(\Delta U/U)$ – amplitude modulation depth, f_m – frequency of signal modulating the amplitude of voltage $u(t)$.

Assuming that voltage $u(t)$ at the input of flickermeter is determined (2), the value of P_{st} indicator depends on the $(\Delta U/U)$ modulation depth and f_m modulating frequency. In literature, one can frequently find $(\Delta U/U) = f(f_m)$ for P_{st}=1 =const (i.e. for the state of flicker perceptibility at each frequency by 50 % of the persons tested). Fig.1. shows that standard characteristic $(\Delta U/U) = f(f_m, P_{st}=1)$ for two nominal voltages: U_n=230 V/f_c=50 Hz and U_n=120 V/f_c=60 Hz was given.

The characteristic in Fig.1. presents three main local minima. The infimum occurs for f_m=8.8 Hz and two local extrema for f_m=91.2 Hz and f_m=108.8 Hz (for f_c=50 Hz). The occurrence of two local minima located close to f_m=100 Hz is sometimes treated as inconsistent with intuitively interpreted operation of flickermeter signal chain. However, the results of analytical calculations and experiments prove that a full characteristic $(\Delta U/U) = f(f_m, P_{st} = \text{const})$ contains three local extrema [53]. It is also valid for characteristic $P_{st} = f(f_m, (\Delta U/U)=\text{const})$, but this one contains three local extrema (a supremum for f_m=8.8 Hz). Characteristic $(\Delta U/U) = f(f_m, P_{st}=\text{const})$ in Fig.1. can be regarded as permissible fluctuation borderline. It means that occurring voltage fluctuations with coordinates $(f_m, (\Delta U/U))$ placed above the borderline can be treated as the occurrence of obnoxious voltage fluctuations.
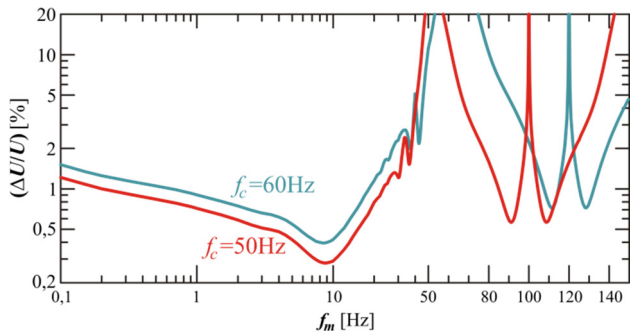
Fig.1. Characteristic ($\Delta U/U$) = f(f_m, P_{st}=1) for U_n=230 V/f_c=50 Hz and U_n=120 V/f_c=60 Hz, amplitude modulation with rectangular signal [53].

3. TESTING OF FLICKER VISION

The vision of flicker was tested in laboratory conditions in a performed measuring stand. The results of this type of tests are susceptible to the conditions in which the tests are carried out. Therefore, it is important to determine a procedure for measurements, lab equipment used and environmental conditions.

The main elements of the measuring stand are: a light source supplied from a generator of voltage fluctuations, lit surface (a sheet of white paper), observer, and operator. The use of white, mat sheet of paper eliminated the specular reflection (of light from the source). Therefore, the observer perceived the flicker of scattered light. Particular elements of the stand were placed in a set position. The light source and lit surface were screened from three sides. The fourth side remained open. Therefore, the observer could easily look at the lit surface. During the measurement, the observer's head was immobilized with a fulcrum applied to the forehead. The light source was screened in such a way that the observer could not see it. The intensity of light reaching the stand was regulated with window roller shades. The operator's task was to manage the tests, including the setting of the f_m frequency and ($\Delta U/U$) modulation depth of AM, and to register the value of threshold flicker vision. The observer's tasks were to focus on the lit surface and to inform the operator when flicker was perceived. A simplified structure of the measuring stand to test flicker vision was shown in Fig.2.
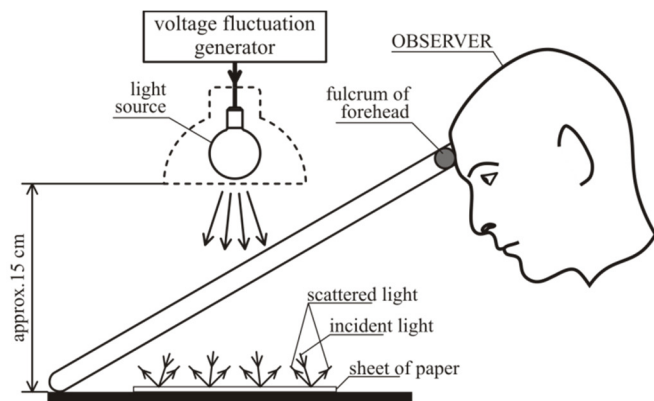
Fig.2. A simplified structure of the measuring stand to test flicker vision.

To generate flicker, a light source supplied from a generator of voltage fluctuations was applied. Five light sources available in the market were applied in the tests: an incandescent bulb with (electric) power of 60 W as well as four LED luminaires: LEDARE, TB, VAKOSS and Samsung. Table 1. gives a statement of basic parameters of these light sources.

Table 1. Statement of basic parameters of the light sources applied in the tests.

No.	Description of light sources	Electric power	Luminous flux
1	Incandescent bulb	60 W	740 lm
2	LEDARE, white 2700K	10 W	600 lm
3	TB LED, neutral white	9 W	800 lm
4	VAKOSS LED, white 2600K	12 W	960 lm
5	Samsung LED, warm white	6 W	810 lm

The conducted laboratory experiments show that for smaller luminous flux the flicker vision is more intense. The tests performed (Table 1.) did not provide the same flux value. However, it was assumed that these differences would not significantly affect flicker vision.

The order of light sources in Table 1. is not identical with the denotations applied in the part of the paper presenting the test results. During the tests, the occurrence of flicker vision for generated voltage fluctuations was not found for one of the LED sources. Therefore, in the presentation of flicker test results this light source was omitted. To generate supply voltage fluctuations, given with dependence (2), light sources with nominal voltage U_n=230 V, a system composed of two main blocks was constructed: function generator Agilent 33512 [54] and generator - calibrator Chroma 61502 [55] (taking the role of power amplifier). A block diagram of the voltage fluctuation generator with added control meters devoted to measure voltage $u(t)$, was shown in Fig.3.

The form of time waveform $u(t)$, according to formula (2), was determined with the settings of generator Agilent 33512. The parameters of voltage fluctuations were set by means of the values of ($\Delta U/U$) modulation depth and f_m frequency of AM with a rectangular signal. The end result of the testing of flicker vision is a set of threshold values ($\Delta U/U$) = f(f_m). In order to determine a threshold value for a set frequency f_m, a minimal value ($\Delta U/U$) = 0.1 % was set preliminarily. Then, the modulation depth was increased as long as flicker was noticed (seen visible). Modulation depth ($\Delta U/U$), corresponding to the detection of flicker, was regarded as the threshold value. For the purpose of these tests, two sets of frequency f_m were assumed: separately for the incandescent light source and for the LED sources. Taking into account the three extrema of characteristic ($\Delta U/U$) = f(f_m, P_{st}=1) (Fig.1.), frequency f_m was divided into three sub-ranges (in relation to the power frequency f_c): **L** ($f_m<f_c$), **H1** ($f_c<f_m<2f_c$) and **H2** ($2f_c<f_m<3f_c$). Full set of f_m frequencies applied in the tests was provided in Table 2.
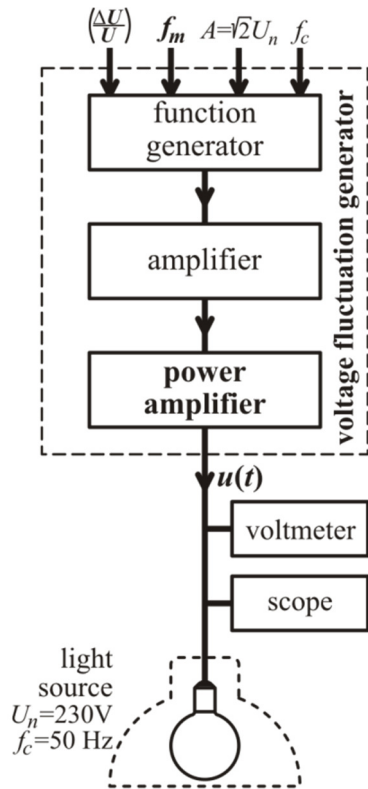
Fig.3. A block diagram of the voltage fluctuation generator with nominal voltage U_n=230 V; function generator – Agilent 33512, amplifier – voltage amplifier with a gain of 4.93 V/V (with op-amp), power amplifier – Chroma 61502, voltmeter – Agilent 34401A, scope – TPS 2024.

Table 2. Statement of f_m frequencies applied in the tests of flicker vision.

Light source	Sub-ranges of f_m [Hz]		
	L	**H1**	**H2**
incandescent bulb	0.1, 0.316, 0.5, 0.916, 2, 4, 6, 7, 8.4, 8.8, 9.2, 10, 11, 12, 13.5, 16, 20, 25, 33.33	88, 90, 91.2, 94, 96	104, 106, 108.8, 110, 112
LEDs	0.1, 1, 2, 5, 8.8, 10, 12, 16, 25	88, 90, 91.2, 94, 96	104, 106, 108.8, 110, 112

A group of 10 volunteers was acquired for the tests – 5 females and 5 males. The tests were carried out in the afternoon (after the volunteers went back from work). Each observer consumed a total test time of 40-50 min. During that time, the observer was staring at a white sheet focusing on the detection of flicker. After some time, it causes fatigue to the observers. The impact of fatigue on the measurement results is not part of the research. However, two observers were twice tested and it obtained converge results from the first and second tests.

A summary of selected information about the observers is given in Table 3. A group of "older people" (4 observers aged between 51 and 53 years) and a group of "younger people" (6 observers aged between 21 and 31 years) were distinguished.

Table 3. Summary of the observers participating in the tests.

No.	Sex	Age	Age group
1	male	53	"older people"
2	male	53	"older people"
3	male	31	"younger people"
4	male	26	"younger people"
5	male	21	"younger people"
6	female	25	"younger people"
7	female	26	"younger people"
8	female	30	"younger people"
9	female	51	"older people"
10	female	52	"older people"

The values obtained in the measurements are binary: the vision of flicker or the lack of flicker vision. Therefore, it is difficult to use statistical tools like the determination of correlation coefficient. That is why the authors did not perform a deeper statistical analysis.

Ten volunteers participating in the tests are not a large statistical sample. However, in the authors' opinion, the results of measurement obtained for such population are sufficiently representative to formulate preliminary conclusions.

4. RESULTS OF EXPERIMENTS ON FLICKER VISION

The result of the tests was a total of 860 threshold values. Fig.4. presents a characteristic $(\Delta U/U)$ = f(f_m) which plotted all the threshold values (for 10 observers and 4 light sources). To make the analysis of the characteristic easier, the permissible fluctuation borderline from Fig.1. was added.
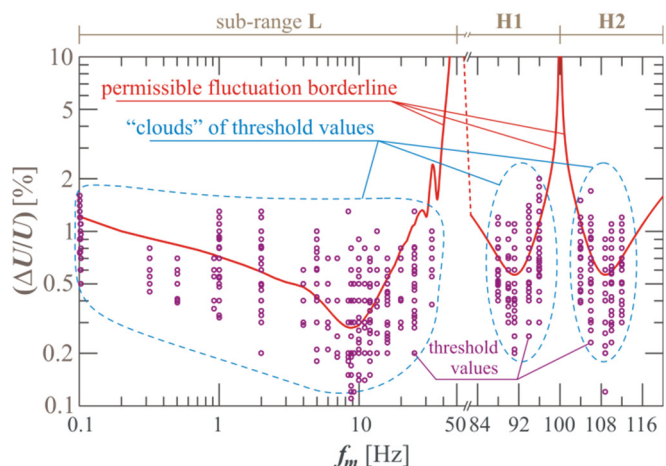
Fig.4. Characteristic $(\Delta U/U)$=f(f_m) with plotted all the threshold values and the standard permissible fluctuation borderline marked.

In the characteristic depicted in Fig.4. one can see "clouds" of points representing the threshold values. The forms of "clouds" of points and the permissible fluctuation borderline indicate a certain degree of similarity. However, the scattered threshold values for particular frequencies f_m suggest that the flicker vision depends not only on frequency f_m, but also on other factors. Therefore, further part of the paper will present the measurement results with regard to the type of source light as well as the age and gender of the observers. As mentioned previously, the permissible fluctuation borderline from Fig.1. describes the perception of flicker for an incandescent source with a power of 60 W. It is justified, then, to compare the obtained results of testing flicker vision with the standard permissible fluctuation borderline.

A. Flicker vision of light emitted by incandescent bulb of 60 W

Because of the availability of standard permissible fluctuation borderline, the testing of flicker vision of light emitted by an incandescent source of 60 W is especially interesting. Fig.5. presents the threshold values for flicker vision for incandescent light source of 60 W. To make the interpretation of the acquired test results easier, the values of modulation depth ($\Delta U/U$) for a particular person and for all frequencies f_m were averaged in the diagram. According to [5], a median was assumed as a feature in the averaging process. Median is widely applied in statistics because it is much more resistant to outliers than arithmetic mean. Its sample value is a consistent and asymptotically unbiased estimator of the expected value in a population for an arbitrary distribution. In all characteristics presented in further parts of the paper, all presented waveforms are determined as averaged values for a tested person with the use of median.
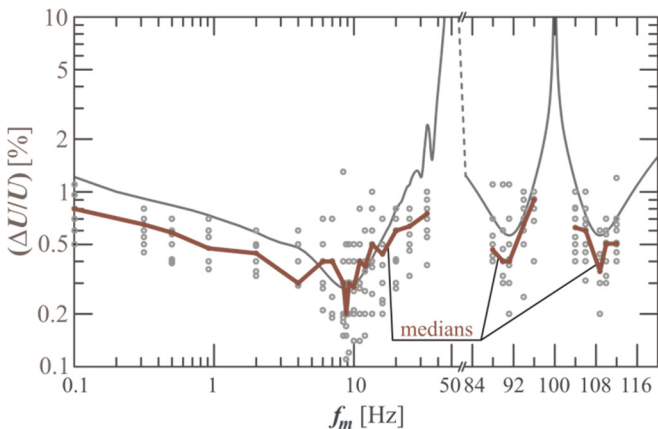
Fig.5.   Characteristic ($\Delta U/U$)=f(f_m) with threshold and median values for incandescent bulb of 60 W and marked permissible fluctuation borderline.

The "clouds" of threshold values in Fig.5. are more similar to the permissible fluctuation borderline than in Fig.4. The location of middle values for most frequencies f_m approximates the form of permissible fluctuation borderline.

The consistency of frequencies corresponding to three local extrema of middle values and permissible fluctuation borderline can be noticed. In order to make a wider comparative analysis, the volunteers who participated in the experiment were divided according to gender and age criteria. The group of observers consisted of 5 females and 5 males. Fig.6. shows the threshold values of flicker vision for incandescent source of 60 W, separately for women and men.

When comparing the characteristics from Fig.6., higher sensitivity to flicker vision can be noticed for female observers. It occurs in three sub-ranges of frequency f_m. Moreover, a group of "younger people" – 6 observers, and a 4-person group of "older people" was formed. A similar analysis was performed as in the case of gender, using as a criterion the age of tested persons. In Fig.7. the threshold values of flicker vision are provided separately for the group of "younger observers" and the group of "older observers".
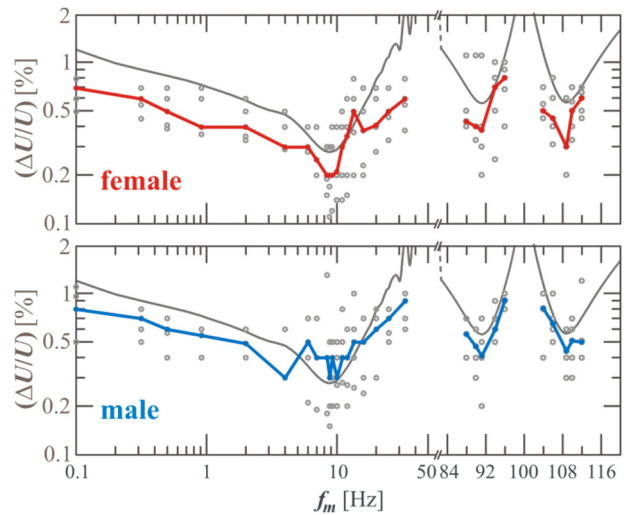
Fig.6.   Characteristic ($\Delta U/U$)=f(f_m) with threshold and median values for incandescent bulb of 60 W; separately for female and male observers.
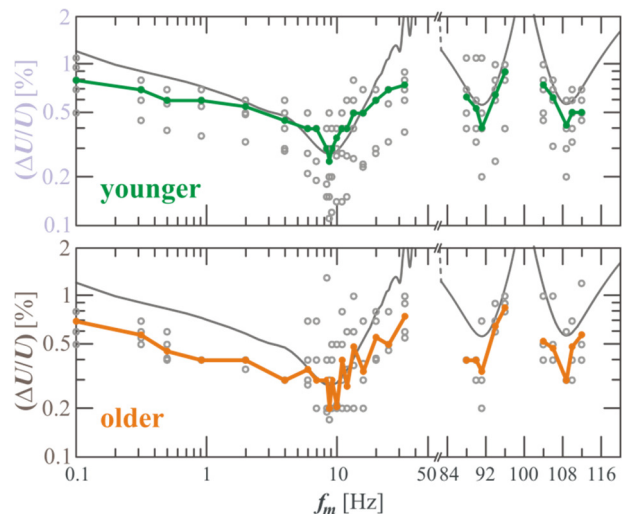
Fig.7.   Characteristic ($\Delta U/U$)=f(f_m) with threshold and median values for incandescent bulb of 60 W; separately for younger and older people.

The test results suggest that older people are more susceptible to flicker of light coming from the incandescent source. Higher susceptibility of older people can be noticed in three sub-ranges of frequency f_m.

B. Flicker vision of light emitted by LED luminaires

Four different LED luminaires were used in the tests. As mentioned before, for one of these sources, flicker was not perceived. At the same time, there was a reference to the results of testing three light sources denoted as LED1, LED2 and LED3, presented below. For comparison, the results of tests for incandescent bulb of 60 W were added. Fig.8. shows the median values of thresholds of flicker vision for sources LED1–LED3 and for a 60 W incandescent bulb.
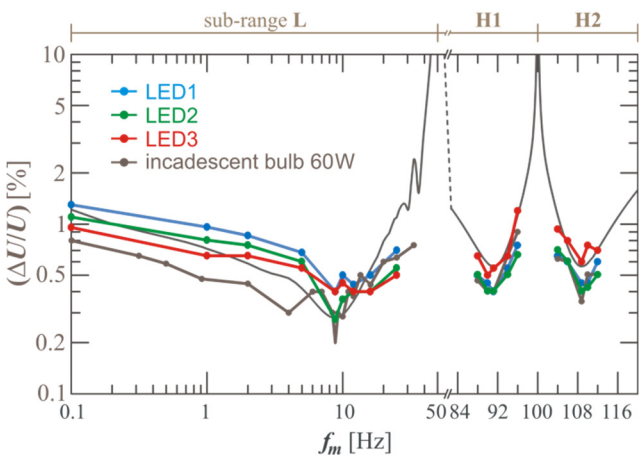
Fig.8. Characteristic $(\Delta U/U)$=f(f_m) with median values of vision thresholds of flicker for LED1 - LED3 luminaires and 60 W incandescent bulb for all observers.

After comparing the test results for different light sources, it can be noticed that for frequency f_m<8.8 Hz, LED sources are less susceptible to voltage fluctuations than incandescent bulbs. Lower susceptibility of LED sources is consistent with intuitive predictions. The reason is that LED luminaires consist of semiconductor light sources (LED diodes) and power supply unit (AC adapter). The susceptibility of LED sources to voltage fluctuations is decided by the properties of supplier (usually the capacity of filter capacitor of AC adapter) [56]-[58]. LED sources without an AC adapter (e.g. LED diodes supplied with a resistor) are the sources of light most susceptible to voltage fluctuations. When analyzing the characteristic in Fig.8. it is easy to notice that in sub-range L, LED3 is the most susceptible from among all the LED sources. Instead, in sub-ranges H1 and H2, this source is the least susceptible to voltage fluctuations. The light spectrum can influence flicker vision. It means that for the same supplier and different LED diodes, flicker vision can also be different.

A comparative analysis of characteristics $(\Delta U/U)$=f(f_m) was also performed for two exemplary LED luminaires, denoted as LED1 and LED3 with regard to the criterion of gender and age. Fig.9. shows the median values of flicker vision (perception) thresholds for sources LED1 and LED3, separately for female and male observers.
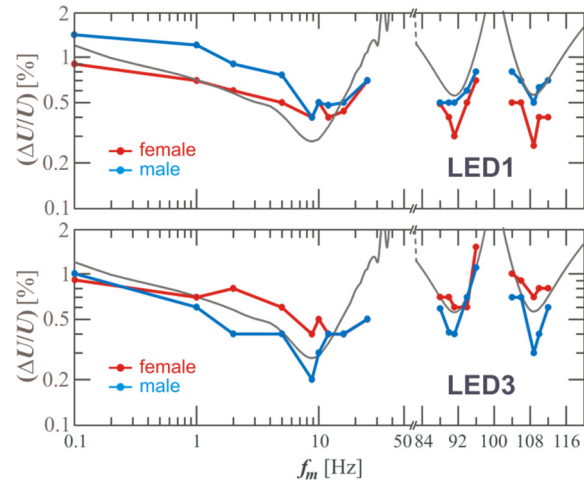
Fig.9. Characteristic $(\Delta U/U)$=f(f_m) with median values of flicker vision thresholds for LED1 and LED3 luminaires; separately for female and male observers.

Fig.10. presents the median values of flicker vision thresholds separately for the group of "younger observers" and the group of "older observers".

Characteristics from Fig.10. show that flicker vision for LED1 and LED3 sources is slightly dependent on the observer's age. In sub-ranges H1 and H2 of frequency f_m the group of younger observers detects flicker slightly easier. In sub-range L it is difficult to indicate a group of observers more susceptible to flicker for LED sources.
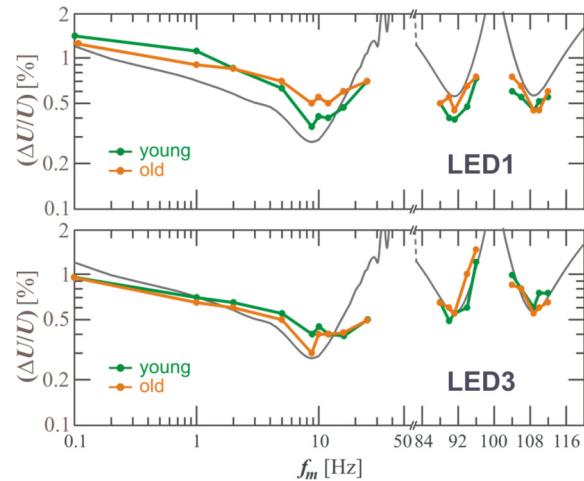
Fig.10. Characteristic $(\Delta U/U)$ = f(f_m) with median values of flicker vision thresholds for LED1 and LED3 luminaires; separately for younger and older observers.

In Fig.4. to Fig.10. a permissible fluctuation borderline is marked ("the reference curve"). This borderline reconstructs the perceptibility threshold of flicker severity found at each frequency by 50 % of the persons tested for a coiled filament gas-filled lamp of 60 W. It is important to emphasize the difference between the perceptibility of flicker severity and the vision of flicker. The medium curve reproduces the threshold of flicker vision. Not every visible flicker is severe. In addition, not every severe flicker of light is visible. From

the previous studies, it is clear that the threshold of flicker vision (for a coiled filament gas-filled lamp of 60 W) is lower than the threshold of flicker severity, regardless of the parameters of the observer.

5. CONCLUSIONS

The paper presents the results of laboratory tests of the dependence of flicker vision on the fluctuations of voltage supplying a selected light source. One incandescent source and four LED sources (different types) were applied in the tests. The measurements were carried out on a properly prepared position measuring stand, on a group of 10 observers. For the purpose of the analysis, the collected test results were divided according to light source type as well as the age and the gender of the observers. During the test while using one of the LED sources, the occurrence of flicker was not found. Thus, only the test results of three LED sources were presented. The tests were carried out in a full frequency range of modulating signal $0 < f_m < 3f_c$ generating flicker. There are no reports of test results in the full modulating frequency range. In the available literature, the testing of flicker vision was limited, without any justification, to the first sub-range of frequency $0 < f_m < f_c$. Analyzing the obtained measurement results, the following conclusions were formulated.

For incandescent light sources, there is a high conformity of frequencies corresponding to local extrema of median values with the permissible fluctuation borderline. When comparing the obtained results according to gender, it is possible to conclude that women are more susceptible to flicker vision than men in all the three sub-ranges of frequency. The results of the tests considering age criterion indicate that the group of "older people" is (only slightly) more susceptible to flicker in comparison with the group of "younger people".

After comparing the test results for different light sources, it can be noticed that, for most part of the L sub-range and whole H1 and H2 sub-ranges, LED sources are less susceptible to voltage fluctuations than incandescent bulbs. Lower susceptibility to voltage fluctuations of LED sources is caused by the fact that the properties of such light sources are decided by the properties of supplier of such source. When comparing the LED sources among one another, one can notice that in sub-range L the most susceptible source is LED3, and in sub-ranges H1 and H2 this source is the least susceptible to voltage fluctuations. In the case of comparative tests of light sources denoted as LED1 and LED3, when dividing the observers according to age and gender, it is possible to formulate two conclusions. Using the criterion of gender, it is possible to state that for LED1 source the group of female observers is more susceptible, and for LED3 source the group of male observers has a higher susceptibility to voltage fluctuations. After the analysis of the obtained results for the groups of "younger people" and "older people", it is possible to conclude that the obtained characteristics do not allow to point out an unequivocal group of observers more susceptible to flicker.

The research results provided in this paper indicate that flicker vision depends on the type of LED source. Therefore,

it is justified to extend the range of experiments for a more numerous population of observers with the use of a bigger number of light sources. The results of tests carried out so far were cognitive. One can, however, perceive their potential utility benefits. For example, trying to decrease the flicker severity, caused by voltage fluctuations, one can replace different light sources with LED sources. However, the susceptibility of LED sources to voltage fluctuations depends on the type. In order to decrease flicker as much as possible, it is necessary to select an appropriate type of LED source. It is also necessary to light the work place in which women dominate with different LED light sources than in the case of lightning the work place for men.

REFERENCES

[1] Braun, J., Perera, S., Gosbell, V. (2005). Design of light chamber for the characterisation of flicker behavior of lamps. In *Australasian Universities Power Engineering Conference*, Hobart, Australia, 1–6.

[2] Chen, S., Heah, M.Y., Then, A.B., Foo, M.K. (2008). Automatic evaluation of flickering sensitivity of fluorescent lamps caused by interharmonic voltages. In *XIII International Conference on Harmonics and Quality of Power*, Wollongong, Australia, 1–6.

[3] Drapela, J., Kratky, M., Weidinger, L., Zavodny, M. (2005). Light flicker of fluorescent lamps with different types of ballasts caused by interharmonics. In *2005 IEEE Russia Power Tech*, St. Petersburg, Russia, 1–7.

[4] International Electrotechnical Commission. (2016). *Voltage fluctuation. IEV number 161-08-05.* http://www.electropedia.org.

[5] International Electrotechnical Commission. (2010). *Testing and measurement techniques – Flickermeter – Functional and design specifications.* IEC 61000-4-15:2010.

[6] Aoki, M. (1980). Standard method for measurement of voltage fluctuations. In *9th International Congress UIE*, Cannes, France, 3–12.

[7] Hong, Y.-Y., Lee, L.-H. (1999). Analysis of equivalent 10 Hz voltage flicker in power systems. *IEE Proceedings - Generation, Transmission and Distribution,* 146 (5), 447–452.

[8] Wiczyński, G. (2017). Model of DV_{10}-meter signal chain for periodic voltage fluctuation. *Measurement*, 93, 224–231.

[9] Owen, E.L. (1994). Power disturbance and power quality – light flicker voltage requirements. In *Conference Record of the 1994 IEEE Industry Applications Society Annual Meeting*, Denver, USA, Vol. 3, 2303–2309.

[10] Wiczyński, G. (2017). Estimation of P_{st} indicator values on the basis of voltage fluctuation indices. *IEEE Transactions on Instrumentation and Measurement*, 66 (8), 2046–2055.

[11] Otomański, P, Wiczyński, G. (2011). The usage of voltage and current fluctuation for localization of disturbing loads supplied from power grid. *Przegląd Elektrotechniczny*, 87 (1), 107–111.

[12] International Electrotechnical Commission. (2016). *Flicker, IEV number 845-02-49*. http://www.electropedia.org.

[13] Lehman, B., Wilkins, A.J. (2014). Designing to mitigate effects of flicker in LED lighting: Reducing risks to health and safety. *IEEE Power Electronics Magazine*, 1 (3), 18–26.

[14] Howarth, P., Heron, G., Greenhouse, D.S., Bailey, I.L., Berman, S.M. (1993). Discomfort from glare: The role of pupillary hippus. *Lighting Research & Technology*, 25 (1), 37–42.

[15] Peretto, L., Rovati, L., Salvatori, G., Tinarelli, R., Emanuel, A.E. (2007). A measurement system for the analysis of the response of the human eye to the light flicker. *IEEE Transactions on Instrumentation and Measurement*, 56 (4), 1384–1390.

[16] Stone, P.T. (2009). A model for the explanation of discomfort and pain in the eye caused by light. *Lighting Research & Technology*, 41 (2), 109–121.

[17] Emanuel, A.E., Peretto, L. (2004). A simple lamp-eye-brain model for flicker observations. *IEEE Transactions on Power Delivery*, 19 (4), 1308–1313.

[18] Peretto, L., Emanuel, A.E. (1997). A theoretical study of the incandescent filament lamp performance under voltage flicker. *IEEE Transactions on Power Delivery*, 12 (1), 279–288.

[19] Peretto, L., Pivello, E., Tinarelli, R., Emanuel, A.E. (2007). Theoretical analysis of the physiologic mechanism of luminous variation in eye-brain system. *IEEE Transactions on Instrumentation and Measurement*, 56 (1), 164–170.

[20] Masi, M.G., Peretto, L., Tinarelli, R., Rovati, L. (2008). Modeling of the physiological behavior of human vision system under flicker condition. In *XIII International Conference on Harmonics and Quality of Power*, Wollongong, Australia, 1–6.

[21] Musiał, E. (2005). Podstawowe pojęcia techniki oświetleniowej. *Biuletyn SEP INPE*, 75. (in Polish)

[22] Kim, C.B., Mayer, M.J. (1994). Foveal flicker sensitivity in healthy aging eyes. II. Cross-sectional aging trends from 18 through 77 years of age. *Journal of the Optical Society of America*, 11 (7), 1958–1969.

[23] Rashbass, C. (1970). The visibility of transient changes of luminance. *Journal of Physiology*, 210 (1), 165–186.

[24] Sokol, S., Tiggs, L.A. (1971). Electrical and psychophysical responses of the human visual system to periodic variation of luminance. *Investigative Ophthalmology*, 10 (3), 171–180.

[25] Wilkins, A., Veitch, J., Lehman, B. (2010). LED lighting flicker and potential health concerns: IEEE standard PAR1789 update. In *IEEE Energy Conversion Congress and Exposition*, Atlanta, USA, 171–178.

[26] Peretto, L., Riva, C.E., Rovati, L., Salvatori, G., Tinarelli, R. (2009). Analysis of the effects of flicker on the blood-flow variation in the human eye. *IEEE Transactions on Instrumentation and Measurement,* 58 (9), 2916–2922.

[27] Cai, R., Cobben, J., Myrzik, J., Blom, J., Kling, W. (2008). New flicker weighting curves for different lamp types based on the lamp light spectrum. In *XIII International Conference on Harmonics and Quality of Power*, Wollongong, Australia, 1–6.

[28] Walker, M. (1979). Electric utility flicker limitations. *IEEE Transactions on Industry Applications*, IA-15 (6), 644–655.

[29] Culham, J.C., Kline, D.W. (2002). The age deficit on photopic counterphase flicker: Contrast, spatial frequency, and luminance effects. *Canadian Journal of Experimental Psychology*, 56 (3), 177–186.

[30] Gallo, D., Landi, C., Pasquino, N. (2006). Design and calibration of an objective flickermeter. *IEEE Transactions on Instrumentation and Measurement*, 55 (6), 2118–2125.

[31] Gallo, D., Landi, C., Pasquino, N. (2004). An instrument for objective measurement of light flicker. *Measurement*, 41 (3), 334–340.

[32] Cai, R., Cobben, J., Myrzik, J., Blom, J., Kling, W. (2009). Flicker responses of different lamp types. *IET Generation, Transmission & Distribution*, 3 (9), 816–824.

[33] Cai, R. (2009). *Working out a model and an analysis of metrological properties of a digital flickermeter*. Ph.D. dissertation, Eindhoven University of Technology, Eindhoven, Netherlands.

[34] Shareef, H., Mohamed, A., Mohamed, K. (2010). Sensitivity of compact fluorescent lamps during voltage sags: An experimental investigation. *WSEAS Transactions on Power Systems*, 1 (5), 22–31.

[35] Masi, M.G., Peretto, L., Tinarelli, R., Rovati, L. (2011). Assessment of human annoyance under flicker condition. In *2011 IEEE Instrumentation and Measurement Technology Conference*, Binjiang, China, 1–5.

[36] Chmielowiec, K. (2011). Flicker effect on different types of light sources. In *11th International Conference on Electrical Power Quality and Utilisation*, Lisbon, Portugal, 1–6.

[37] Azcarate, I., Gutierrez, J., Saiz, P., Lazkano, A., Leturiondo, L., Redondo, K. (2014). Flicker characteristics of efficient lighting assessed by the IEC flickermeter. *Electric Power Systems Research*, 107, 21–27.

[38] Azcarate, I., Gutierrez, J., Lazkano, A., Saiz, P., Redondo, K., Leturiondo, L. (2014). Experimental study of the response of efficient lighting technologies to complex voltage fluctuations. *Electrical Power and Energy Systems*, 63, 499–506.

[39] International Electrotechnical Commission. (2015). *Testing and measurement techniques – Power Quality Measurement Methods*. IEC 61000-4-30:2015.

[40] de Lange Dzn, H. (1958). Research into the dynamic nature of the human fovea - cortex systems with intermittent and modulated light. II. Phase shift in brightness and delay in color perception. *Journal of the Optical Society of America*, 48 (11), 784–789.

[41] Kelly, D.H. (1961). Visual responses to time-dependent stimuli. I. Amplitude sensitivity measurements. *Journal of the Optical Society of America*, 51 (4), 422–429.

[42] Andersson, N., Sandstrom, M., Berglund, A., Hansson, K. (1994). Amplitude modulation of light various sources. *Lighting Research and Technology*, 26 (3), 157–160.

[43] Veitch, J.A., McColl, S.L. (1995). Modulation of fluorescent light: Flicker rate and light source effects on visual performance and visual comfort. *Lighting Research and Technology*, 27 (4), 243–256.

[44] Carrillo, C., Cidrás, J. (2001). Fluorescent lamp modelling for voltage fluctuations. *European Transactions on Electrical Power*, 11 (2), 119–127.

[45] Gomez, J., Morcos, M. (2002). Flicker measurement and light effect. *IEEE Power Engineering Review*, 22 (11), 11–15.

[46] Rong, C., Cobben, J.F.G., Myrzik, J.M.A., Blom, J.H., Kling, W.L. (2007). Flickermeter used for different types of lamps. In *9th International Conference on Electrical Power Quality and Utilisation*, Barcelona, Spain, 1–6.

[47] Manana, M., Ortiz, A., Renedo, C., Perez, S., Delgado, F., Azcondo, F.J., Diaz, F.J., Branas, C., Casanueva, R. (2007). Comparison of flicker sensitivity in HPS lamps. In *International Symposium on Industrial Electronics*, Vigo, Spain, 3002–3007.

[48] Wie, Z., Watson, N.R., Frater, L.P. (2008). Modelling of compact fluorescent lamps. In *XIII International Conference on Harmonics and Quality of Power*, Wollongong, Australia, 1–6.

[49] Kim, T., Rylander, M., Powers, E.J., Grady, W.M., Arapostathis, A. (2008). LED lamp flicker caused by interharmonics. In *IEEE International Instrumentation and Measurement Technology Conference*, Victoria, Canada, 1–6.

[50] Koponen, P, Hansen, H., Bollen, M. (2015). Interharmonics and light flicker. In *23rd International Conference on Electricity Distribution*, Lyon, France, 1/5−5/5.

[51] Wang, C. (2008). Flicker-insensitive light dimmer for incandescent lamps. *IEEE Transactions on Industrial Electronics*, 55 (2), 767–772.

[52] Sharma, H., Sharp, F., McGranaghan, M. (2013). Flicker voltage fluctuation response of modern lamps including those with dimmable capability and other low voltage sensitive equipment. In *22nd International Conference on Electricity Distribution*, Stockholm, Sweden, 1–4.

[53] Wiczyński, G. (2008). Sectional approximation of the flickermeter transformation characteristic for a sinusoidal modulating signal. *IEEE Transactions on Instrumentation and Measurement*, 57 (10), 2355–2363.

[54] Agilent Technologies, Inc. (2012). *Agilent 33500 Series Waveform Generator - Operating and Service Guide.*

[55] Chroma ATE Inc. (2004). *Programmable AC Source 61501/61502/61503/61504 User's Manual.*

[56] Uddin, S., Shareef, H., Mohamed, A. (2013). Power quality performance of energy-efficient low-wattage LED lamps. *Measurement*, 46 (10), 3783-3795.

[57] Zhang, R., Chung, H.S. (2014). A triac-dimmable LED lamp driver with wide dimming range. *IEEE Transactions on Power Delivery*, 29 (3), 1434–1446.

[58] Shrivastava, A., Singh, B., Pal, S. (2015). A novel wall-switched step-dimming concept in LED lighting systems using PFC zeta converter. *IEEE Transactions on Industrial Electronics*, 62 (10), 6272–6283

MEASUREMENT SCIENCE REVIEW

An Improved Linearization Circuit Used for Optical Rotary Encoders

Jelena Jovanović[1], Dragan Denić[1], Uglješa Jovanović[2]

[1]*Department of Measurements, Faculty of Electronic Engineering, University of Niš, Aleksandra Medvedeva, 14, 18000, Niš, Serbia, jelena.jovanovic@elfak.ni.ac.rs*
[2]*Department of Electronics, Faculty of Electronic Engineering, University of Niš, Aleksandra Medvedeva, 14, 18000, Niš, Serbia*

Optical rotary encoders generate nonlinear sine and cosine signals in response to a change of angular position that is being measured. Due to the nonlinear shape of encoder output signals, encoder sensitivity to very small changes of angular position is low, causing a poor measurement accuracy level. To improve the optical encoder sensitivity and to increase its accuracy, an improved linearization circuit based on pseudo-linear signal generation and its further linearization with the two-stage piecewise linear analog-to-digital converter is presented in this paper. The proposed linearization circuit is composed of a mixed-signal circuit, which generates analog pseudo-linear signal and determines the first four bits of the final digital result, and the two-stage piecewise linear analog-to-digital converter, which performs simultaneous linearization and digitalization of the pseudo-linear signal. As a result, the maximal value of the absolute measurement error equals to $3.77168 \cdot 10^{-5}$ [rad] (0.00216°) over the full measurement range of 2π [rad].

Keywords: Angular position measurement, linearization, analog-to-digital conversion, accuracy improvement.

1. INTRODUCTION

In this paper, attention is devoted to the linearization of optical rotary encoder output signals by using an improved linearization circuit, which, in general, can be applied to other types of sensors with sinusoidal output signals, i.e. with magnetic sensors, resolvers [1]-[5], and sensors based on the Hall effect [6]. The application of the proposed linearization circuit overcomes the disadvantages of processor demanding digital techniques, while at the same time represents a more flexible solution in comparison to analog linearization techniques [7]. In [1], [2], the angular position determination method based on the knowledge of the resolver excitation signal amplitude is proposed. In particular, this method is based on a comparison between amplitudes of the pseudo-linear signal and the resolver excitation signal, so the additional errors, caused by the fluctuation and drift of the excitation signal amplitude are introduced. In paper [3], in order to obtain a signal that is as close as possible to an ideal triangular signal, the linearization of a signal representing a difference between the absolute values of demodulated resolver output signals is performed. As a result, for determination of the angular position, simpler linear equations can be used. However, the application of rectifying circuits for the resolver linearization leads to the introduction of additional nonlinearities. All the above-mentioned disadvantages can be avoided by using the linearization technique proposed in this paper.

The linearization technique proposed in this paper includes two phases: 1. generation of a pseudo-linear signal and the first four bits of the final digital result; and 2. simultaneous linearization and digitalization of the pseudo-linear signal.

2. PROPOSED LINEARIZATION CIRCUIT

The proposed linearization circuit is composed of two circuits: 1. a special-purpose 4-bit mixed-signal circuit used for pre-processing of co-sinusoidal signals in order to generate the pseudo-linear signal and the first four bits of the final digital result; and 2. a two-stage piecewise linear A/D converter (TSPLADC) used for simultaneous linearization and digitalization of the pseudo-linear signal obtained at the mixed-signal circuit output. The TSPLADC is a general-purpose linearization circuit, i.e. by reprogramming its transfer function any sensor type can be linearized [8]-[15].

Fig.1. shows the block diagram of the mixed-signal circuit. By observing Fig.1., one can notice three building blocks of the circuit: an analog signals generating block, a block for the generation of the first four bits of the final digital result (D_{n-1}, D_{n-2}, D_{n-3} and D_{n-4}, where n stands for the overall resolution $n=4+N_1+N_2$, including resolutions N_1 and N_2 of the first and the second conversion stage of the TSPLADC, respectively), and a 16 to 1 analog multiplexer (AMUX), which is controlled by the four generated bits.
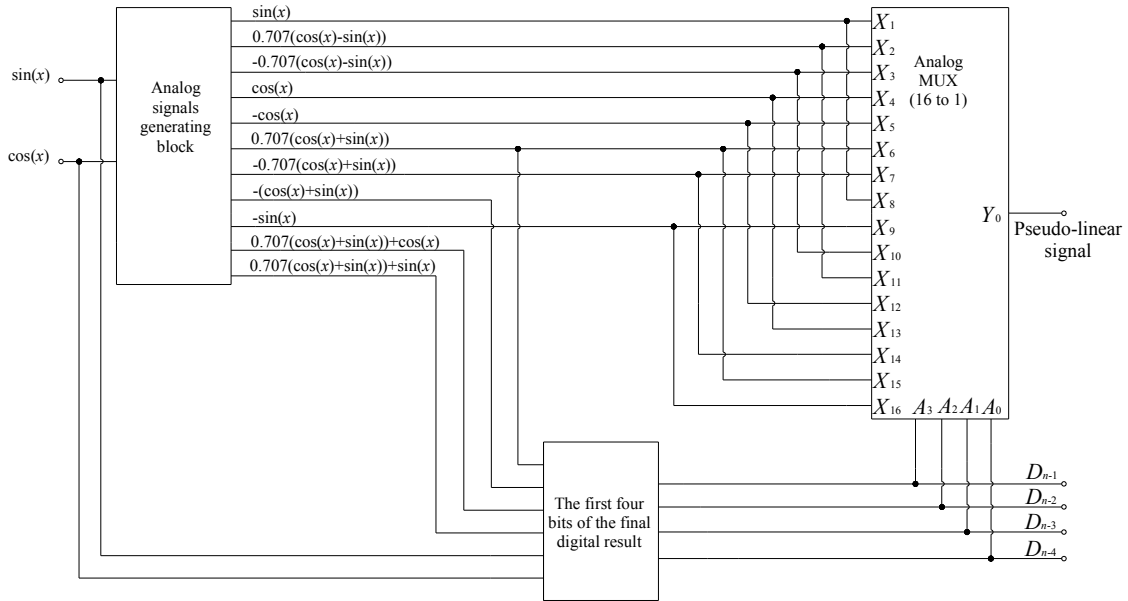
Fig.1. Block diagram of the 4-bit mixed-signal circuit used for the pseudo-linear signal generation.
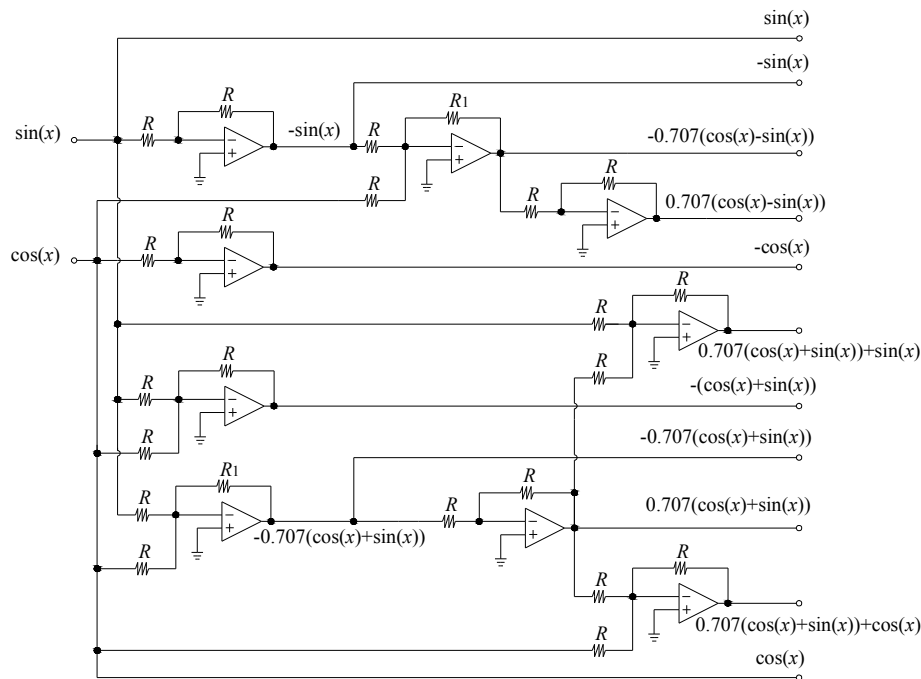
Fig.2. Analog signals generating block.

A detailed schematic of the analog signals generating block is shown in Fig.2. The circuit is comprised of operational amplifiers and required resistors R=1 kΩ and R_1=0.707 kΩ. The resistor R_1 represents, in fact, a serial connection between two resistors: 680 Ω and 27 Ω.

In order to clarify the reason why these analog signals are needed, in Fig.3. are shown their waveforms together with the pseudo-linear signal waveform (bolded line). These waveforms are obtained by simulating the proposed mixed-signal circuit in the LabVIEW software. Signals representing

the sum of, or the difference between, sine and cosine signals multiplied by 0.707 (or $\sqrt{2}/2$) are obtained by phase shifting the sine and cosine signal for π/4 [rad], while the signals representing the sum of, or the difference between, sine and cosine signal multiplied by -0.707 (or $-\sqrt{2}/2$) are obtained by inverting the sine and cosine signal phase shifted for π/4 [rad]. Signals, which exhibit a higher level of linearity in certain segments (π/8 [rad] wide) in comparison to the original co-sinusoidal signals, are obtained in this manner. The pseudo-linear signal amplitude is equal to:

$\sin(\pi/8)\cdot A=0.383\cdot A$ [V], where A [V] stands for the amplitude of co-sinusoidal signals.

The pseudo-linear signal represents a combination of the most linear fragments of eight analog signals shown in Fig.2. and Fig.3. These are the following signals:

$$S_1 = \sin(x), \tag{1}$$

$$S_2 = \cos\left(x+\frac{\pi}{4}\right) = \frac{\sqrt{2}}{2}\left(\cos(x)-\sin(x)\right), \tag{2}$$

$$S_3 = -\cos\left(x+\frac{\pi}{4}\right) = -\frac{\sqrt{2}}{2}\left(\cos(x)-\sin(x)\right), \tag{3}$$

$$S_4 = \cos(x), \tag{4}$$

$$S_5 = -\cos(x), \tag{5}$$

$$S_6 = \sin\left(x+\frac{\pi}{4}\right) = \frac{\sqrt{2}}{2}\left(\cos(x)+\sin(x)\right), \tag{6}$$

$$S_7 = -\sin\left(x+\frac{\pi}{4}\right) = -\frac{\sqrt{2}}{2}\left(\cos(x)+\sin(x)\right), \tag{7}$$

$$S_8 = -\sin(x). \tag{8}$$
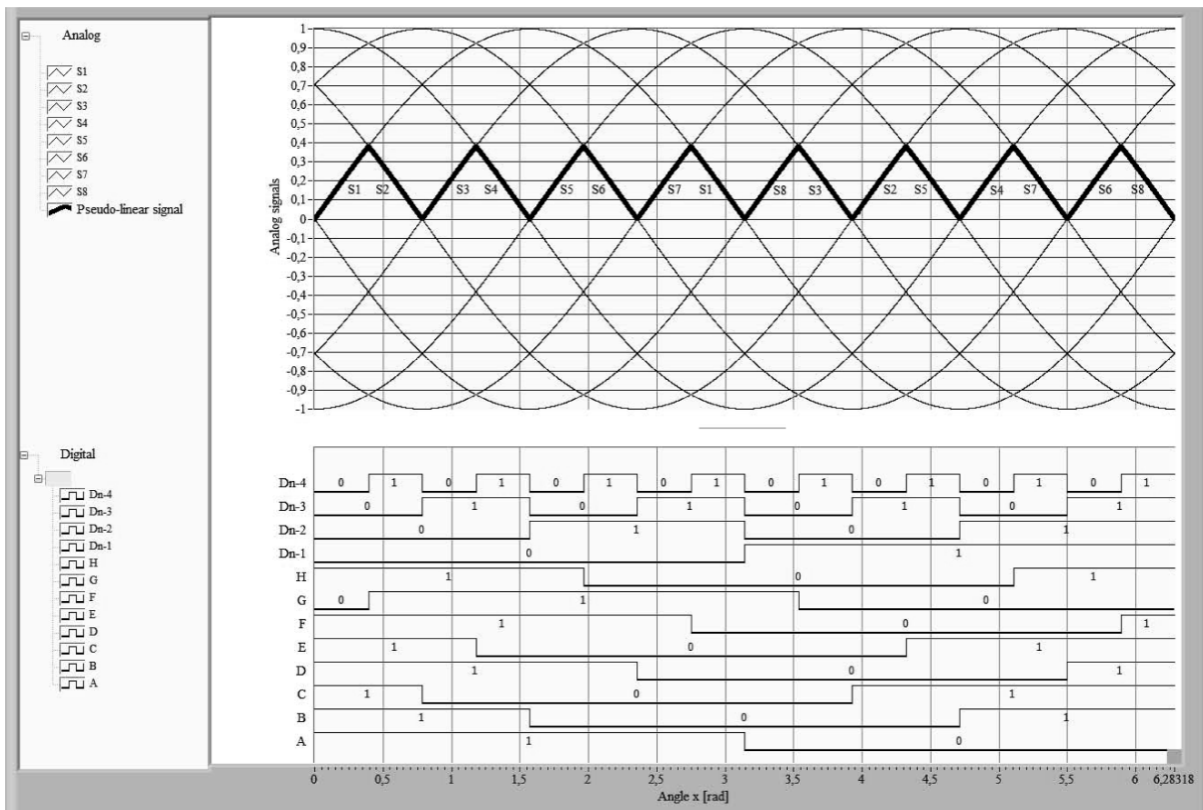
Fig.3. Analog and digital signals in different points of the mixed-signal circuit.

Each of these signals appears two times at the AMUX output, meaning that the pseudo-linear signal is composed of 16 fragments in the range from 0 to 2π [rad]. Which fragment is obtained at the AMUX output is determined by the bits D_{n-1}, D_{n-2}, D_{n-3} and D_{n-4}, generated by the circuit shown in Fig.4. Additionally, the circuit shown in Fig.2. generates three signals (S_6+S_4, S_6+S_1, $-(S_1+S_4)$) that are not used for pseudo-linear signal generation, but are essential for the determination of bits D_{n-1}, D_{n-2}, D_{n-3} and D_{n-4}.

Digital signals A, B, C, D, E, F, G and H (Fig.4.) represent the results of comparisons given in Table 1.

Table 1. Digital signals generated in order to obtain the first four bits of the final digital result.

Digital signal	Comparison
A	$\sin(x)>0$
B	$\cos(x)>0$
C	$\cos(x)>\sin(x)$
D	$\cos(x)+\sin(x)>0$
E	$0.707(\cos(x)+\sin(x))>\sin(x)$
F	$0.707(\cos(x)+\sin(x))+\sin(x)>0$
G	$0.707(\cos(x)+\sin(x))>\cos(x)$
H	$0.707(\cos(x)+\sin(x))+\cos(x)>0$
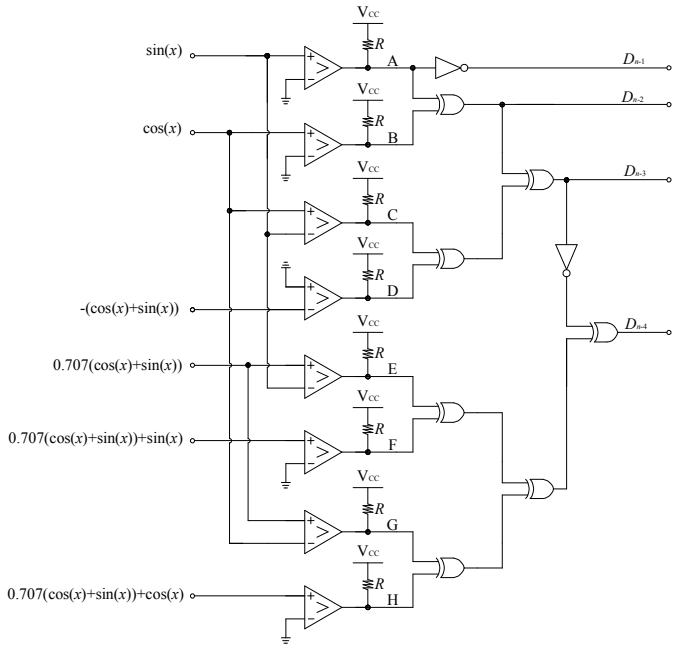
Fig.4. The block for the generation of the first four bits of the final digital result.

By conducting simple logical operations over digital signals (A…H), the bits D_{n-1}, D_{n-2}, D_{n-3} and D_{n-4} are generated:

$$D_{n-1} = \overline{A}, \tag{9}$$

$$D_{n-2} = A \, \text{XOR} \, B, \tag{10}$$

$$D_{n-3} = (A \, \text{XOR} \, B) \, \text{XOR} \, (C \, \text{XOR} \, D), \tag{11}$$

$$D_{n-4} = ((E \, \text{XOR} \, F) \, \text{XOR} \, (G \, \text{XOR} \, H)) \, \text{XOR} \, \overline{D}_{n-3}. \tag{12}$$

As it can be seen from Table 1., in order to generate digital signals (A…H) no additional reference voltage is used, as it is proposed in [1], [2], where it consequently led to the introduction of additional errors.

Since the pseudo-linear signal has the shape of $\sin(x)$ signal in each segment (see Fig.3.), it is sufficient to linearize $\sin(x)$ signal within one segment and have the information about that segment (bits D_{n-1}, D_{n-2}, D_{n-3}, D_{n-4}). As a result, linearization of the pseudo-linear signal with the TSPLADC is always performed within one segment. However, the slope of the pseudo-linear signal is negative in even segments, so in order to obtain a linear and monotonically rising transfer function, inversion of bits D_0-D_{n-5} is necessary in even segments. The inversion is performed by bringing the bits D_0-D_{n-5} to the inputs of XOR circuits together with the bit D_{n-4} (see Fig.5.).
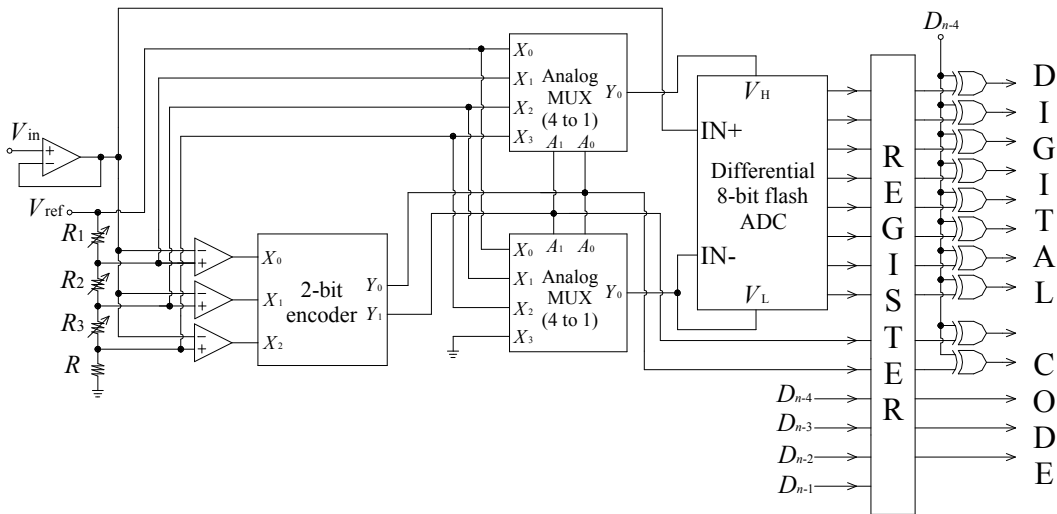
Fig.5. The two-stage piecewise linear analog-to-digital converter (TSPLADC).

The TSPLADC performs two conversion stages. The first conversion stage is performed by the piecewise linear flash A/D converter (ADC) having the input range non-uniformly divided into regions of unequal width in order to better approximate the function inverse to the dependence of the pseudo-linear voltage on the measured angle. In this manner, the non-linearity of pseudo-linear signal is compensated. The flash ADC employed in the second conversion stage is linear and it does not perform linearization. However, it reduces the quantization noise introduced in the signal during the first conversion stage, which in a smaller percentage reduces the

overall measurement error. The input range of the second conversion stage is defined by the boundaries of the non-uniform region determined in the first conversion stage, and to which the current value of the measured angle belongs.

In the example shown in Fig.5., the first conversion stage is with the resolution of N_1=2 bits. For the realization of the 2-bit flash ADC a network of four resistors is needed in order to adjust the reference voltages of the comparators. Since the circuit proposed in this paper is intended just for the linearization of the optical rotary encoder, the reference voltages, i.e. so-called break voltages, are set only once by

using the variable resistors R_1, R_2 and R_3. The break voltages V_i, determined in the following manner:

$$V_i = \sin\left(i \cdot \frac{1}{2^{N_1}} \cdot \frac{\pi}{8}\right), i=1, 2,\ldots, 2^{N1}\text{-}1, \qquad (13)$$

represent the boundaries of the non-uniform regions that compose the first stage flash ADC input range. Different solutions of the TSPLADC used for sensor linearization have been proposed during time, and among them are some that are considered as energy efficient [14], [15].

3. SIMULATION AND NUMERICAL RESULTS

The proposed 4-bit mixed-signal circuit is simulated using the Multisim software. Also, the overview of numerical results concerning the proposed circuit and their comparison with the corresponding parameters obtained using the previous version of the proposed circuit are given. The previous version of the linearization circuit is composed of the 3-bit mixed-signal circuit and the TSPLADC of the same design as the one described in this paper. In both cases the numerical results are generated using the LabVIEW software.

The simulation is an important indicator that the newly designed circuit is going to work as expected. Therefore, the simulation is a preceding step to the realization of a newly designed circuit which can prevent the loss of funds and time if there is an error in the circuit design. For the Multisim simulation of the proposed 4-bit mixed-signal circuit, commercially available components are used: LM224N operational amplifiers, LM239D comparators, 4030BT logical XOR circuits, 4049BD HEX inverting buffers, ADG406BN analog multiplexer, and adequate voltage supplies and resistors. Fig.6. shows simulation scope shoot of sine and cosine inputs and the AMUX output signal. The sine (yellow, CH1), cosine (blue, CH2), and pseudo-linear (green, CH4) signal from Fig.6. fully correspond to the expected theoretical results shown in Fig.3.

The simulation results obtained in Multisim can be closely considered as experimental due to the fact that the simulation is carried out using commercially available components. Therefore, it can be expected that the realization of the proposed 4-bit mixed-signal circuit, with the same components, will function in agreement with theory.
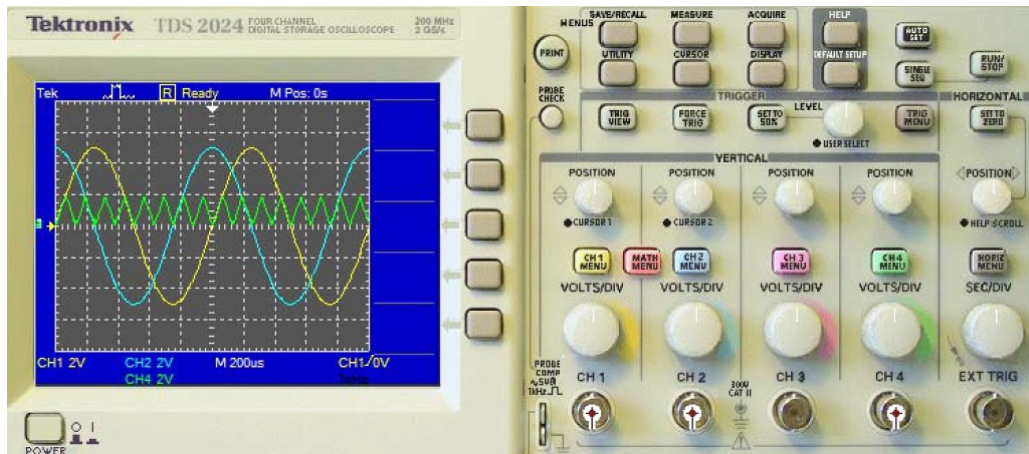
Fig.6. Scope shoot of sine (yellow, CH1) and cosine (blue, CH2) inputs, and the AMUX output signal (green, CH4) for the proposed 4-bit mixed-signal consisting of commercially available components.

The assessment of the performances and the comparison of the proposed linearization circuit to its previous version containing the 3-bit mixed-signal circuit [12], are performed based on the values of the following parameters: the maximal value of the absolute measurement error Δx [rad] and the value of nonlinearity δx [%], which are defined by the expressions (14) and (15), respectively:

$$\Delta x[\text{rad}] = \left|x_{\text{out}} - x_{\text{in}}\right|, \qquad (14)$$

$$\delta x[\%] = \frac{\Delta x_{\text{max}}[\text{rad}]}{2\pi[\text{rad}]} \cdot 100\%. \qquad (15)$$

Two parameters are figuring in the expression (14): x_{in} [rad], which represents the actual, or the correct value of the measured angle x that is fed to the encoder input, and x_{out} [rad], which represents the output, i.e. the measured value of angle x after the linearization is finished. In the expression (15), Δx_{max} [rad] represents the maximal value of the absolute measurement error, while 2π [rad] denotes the full measurement range [16].

By using the LabVIEW software, two measurement system solutions were examined: one, with the proposed linearization circuit, and one with its previous version [12]. In the virtual instrument, which in addition to the mixed-signal circuit (3-bit or 4-bit), simulates the TSPLADC function, the parameter x_{in} is predefined, while the

parameter x_{out} is calculated. Thus, the virtual instrument determines the value of x_{out} as a function of: 1. x_{in} value; 2. the mixed-signal circuit resolution; 3. the pseudo-linear signal amplitude (which in case the 3-bit mixed-signal circuit is employed equals to $0.707 \cdot A$ [V], [12]); and 4. the resolutions of the first and the second conversion stage.

In Table 2. to Table 5., the maximal value of the absolute measurement error and the nonlinearity value, for different combinations of resolutions N_1 and N_2, are given. The resolutions denoted with N_1' and N_2' refer to the solution with the 3-bit mixed-signal circuit, while the resolutions denoted with N_1'' and N_2'' refer to the solution with the 4-bit mixed-signal circuit. The following cases were investigated:

Case 1 is illustrated in Table 2., in which the performances of both linearization circuits are given. Both solutions employ the TSPLADC of the same resolution in both conversion stages ($N_1'=N_1''$, $N_2'=N_2''$);

Case 2 is illustrated in Table 3. and represents a situation in which the first conversion stage of the TSPLADC does

not perform the linearization, while the second conversion stage resolutions for both solutions are mutually equal ($N_1'=N_1''=0$, $N_2'=N_2''$);

Case 3 is illustrated in Table 4. and represents a situation in which the first conversion stage of the TSPLADC does not perform the linearization, while the overall resolutions of both solutions are mutually equal ($N_1'=N_1''=0$, $3+N_2'=4+N_2''$, i.e. $N_2'=1+N_2''$);

Case 4 is illustrated in Table 5. and represents a situation in which the overall resolutions of both linearization circuit solutions are mutually equal, whereby the first stage resolution N_1' is 1 bit higher than the resolution N_1'' ($N_1'=1+N_1''$, $3+N_1'+N_2'=4+N_1''+N_2''$).

These cases are analyzed in order to understand whether a greater reduction of the maximal absolute measurement error and nonlinearity is achieved by increasing the mixed-signal circuit resolution or by increasing the first conversion stage resolution, since both circuits perform linearization. Additionally, the aforementioned circuits' complexities increase disproportionately to the resolution.

Table 2. Case 1 ($N_1'=N_1''$, $N_2'=N_2''$).

3-bit mixed-signal circuit				4-bit mixed-signal circuit				Improvement ratio
N_1'	N_2'	$\Delta x_{max}'$ [rad]	$\delta x'$ [%]	N_1''	N_2''	$\Delta x_{max}''$ [rad]	$\delta x''$ [%]	$\Delta x_{max}'/\Delta x_{max}''$, $\delta x'/\delta x''$
0	16	0.0331395	0.527432	0	16	0.0039538	0.0629266	8.381683
2	6	0.00849212	0.135156	2	6	0.00265563	0.0422656	3.19778
2	8	0.00506459	0.0806055	2	8	0.000998315	0.0158887	5.073138
2	10	0.00423256	0.0673633	2	10	0.000570334	0.00907715	7.421195
2	12	0.00402371	0.0640393	2	12	0.000464183	0.0073877	8.66837
2	14	0.00397232	0.0632214	2	14	0.000439342	0.00699234	9.041521
3	8	0.00162663	0.0258887	3	8	0.000388711	0.00618652	4.184677
3	10	0.00122258	0.019458	3	10	0.000183311	0.00291748	6.669431
3	12	0.0011233	0.0178778	3	12	0.000131922	0.00209961	8.51488
3	14	0.00109762	0.0174692	3	14	0.000119521	0.00190224	9.183491
4	8	0.000568493	0.00904785	4	8	0.000169658	0.0027002	3.350817
4	10	0.000349364	0.0055603	4	10	6.35068E-5	0.00101074	5.501206
4	12	0.000303134	0.00482452	4	12	3.77168E-5	0.000600281	8.037108

Table 3. Case 2 ($N_1'=N_1''=0$, $N_2'=N_2''$).

3-bit mixed-signal circuit				4-bit mixed-signal circuit				Improvement ratio
N_1'	N_2'	$\Delta x_{max}'$ [rad]	$\delta x'$ [%]	N_1''	N_2''	$\Delta x_{max}''$ [rad]	$\delta x''$ [%]	$\Delta x_{max}'/\Delta x_{max}''$, $\delta x'/\delta x''$
0	6	0.0513454	0.817188	0	6	0.0131063	0.208594	3.917612
0	8	0.0376697	0.599531	0	8	0.00615556	0.0979688	6.119622
0	10	0.0342421	0.54498	0	10	0.00449825	0.0715918	7.612316
0	12	0.0333929	0.531465	0	12	0.00408392	0.0649976	8.176678
0	14	0.0331943	0.528304	0	14	0.00397777	0.0633081	8.344952
0	16	0.0331395	0.527432	0	16	0.0039538	0.0629266	8.381683

Table 4. Case 3 ($N_1'=N_1''=0$, $3+N_2'=4+N_2''$, i.e. $N_2'=1+N_2''$).

3-bit mixed-signal circuit				4-bit mixed-signal circuit				Improvement ratio
N_1'	N_2'	$\Delta x_{max}'$ [rad]	$\delta x'$ [%]	N_1''	N_2''	$\Delta x_{max}''$ [rad]	$\delta x''$ [%]	$\Delta x_{max}'/\Delta x_{max}''$, $\delta x'/\delta x''$
0	7	0.0422544	0.6725	0	6	0.0131063	0.208594	3.223976
0	9	0.0354165	0.563672	0	8	0.00615556	0.0979688	5.753579
0	11	0.0336703	0.535879	0	10	0.00449825	0.0715918	7.4852
0	13	0.0332628	0.529395	0	12	0.00408392	0.0649976	8.144822
0	15	0.0331601	0.527759	0	14	0.00397777	0.0633081	8.336354
0	17	0.0331318	0.52731	0	16	0.0039538	0.0629266	8.379736

Table 5. Case 4 ($N_1'=1+N_1''$, $3+N_1'+N_2'=4+N_1''+N_2''$).

3-bit mixed-signal circuit				4-bit mixed-signal circuit				Improvement ratio
N_1'	N_2'	$\Delta x_{max}'$ [rad]	$\delta x'$ [%]	N_1''	N_2''	$\Delta x_{max}''$ [rad]	$\delta x''$ [%]	$\Delta x_{max}'/\Delta x_{max}''$, $\delta x'/\delta x''$
1	16	0.01296	0.206265	0	16	0.0039538	0.0629266	3.27786
3	6	0.00328395	0.0522656	2	6	0.00265563	0.0422656	1.236599
3	8	0.00162663	0.0258887	2	8	0.000998315	0.0158887	1.629375
3	10	0.00122258	0.019458	2	10	0.000570334	0.00907715	2.143621
3	12	0.0011233	0.0178778	2	12	0.000464183	0.0073877	2.419951
3	14	0.00109762	0.0174692	2	14	0.000439342	0.00699234	2.498327
4	8	0.000568493	0.00904785	3	8	0.000388711	0.00618652	1.462508
4	10	0.000349364	0.0055603	3	10	0.000183311	0.00291748	1.905854
4	12	0.000303134	0.00482452	3	12	0.000131922	0.00209961	2.297827
4	14	0.000289443	0.00460663	3	14	0.000119521	0.00190224	2.421692
5	8	0.000212456	0.00338135	4	8	0.000169658	0.0027002	1.25226
5	10	0.00010619	0.00169006	4	10	6.35068E-5	0.00101074	1.672104
5	12	8.05148E-5	0.00128143	4	12	3.77168E-5	0.000600281	2.13472

Case 1: By comparing measurement error and nonlinearity values given in Table 2., a significant improvement is observed in the case when the 4-bit mixed-signal circuit is employed. The improvement is defined as the ratio between $\Delta x_{max}'$ and $\Delta x_{max}''$, or between $\delta x'$ and $\delta x''$. The improvement ratio higher than 1 implies that the linearization circuit proposed in this paper shows better performances in comparison to the solution proposed in [12]. A difference between $\Delta x_{max}'$ and $\Delta x_{max}''$ is greater when the resolution of the TSPLADC is higher.

Case 2: In this case, resolutions N_1' and N_1'' are equal to 0 meaning that the linearization is not performed with the TSPLADC. The improvement ratio increases with the increase of the second stage resolution. This case is a sub-case of Case 1, which is singled out in order to observe the influence of the second stage resolution on the linearization circuit performances.

Case 3: In this case, the same as in Case 2, the linearization by the first conversion stage is not performed, i.e. $N_1'=N_1''=0$. However, in this case the resolution N_2' is 1 bit higher than N_2'', resulting in lower improvement ratios in comparison to Case 2. Although the overall resolutions for both solutions are the same, the solution employing the 4-bit mixed-signal circuit has better performances because the improvement

ratio is higher than 1. This is the case when the influence of the mixed-signal circuit resolution on the linearization circuit performances is singled out.

Case 4: In this case, although the resolution N_1' is 1 bit higher than N_1'', better performances are achieved using the linearization circuit with the 4-bit mixed-signal circuit. From here, one can conclude that the main contribution to the nonlinearity reduction and accuracy improvement is achieved using the 4-bit mixed-signal circuit. In other words, higher resolution of the mixed-signal circuit has provided the greatest improvement in the optical rotary encoder accuracy. The previous statement justifies the need for a certain level of complexity increase of the mixed-signal circuit used for the pseudo-linear signal generation. However, the improvement ratio in this case has the lowest values due to the fact that the resolution N_1' is 1 bit higher than N_1''. Continuation of the resolution N_1' increase leads to the improvement of performances of the linearization circuit with the 3-bit mixed-signal circuit. However, high resolution of the first conversion stage makes the piecewise linear flash ADC complexity high, i.e. a large number of non-uniform break (reference) voltages needs to be calculated and adjusted using more components, such as variable resistors. In addition, each time the flash ADC resolution increases by 1 bit the number

of employed comparators doubles making their matching and proper biasing more difficult [17]. Also, the complexity and the power consumption of the ADC are increased. In other words, it is preferable to exploit the 4-bit mixed-signal circuit than to increase the resolution of the first stage flash ADC. When both linearization circuit solutions have the same overall resolution, the lower measurement error is achieved with a circuit having the mixed-signal circuit with higher resolution than the circuit having the first conversion stage with higher resolution (see Table 5.).

To realize all the benefits of the linearization circuit proposed in this paper it is important to compare it with other linearization solutions proposed in the literature. The paper [6] describes a converter that is using alternating pseudo-linear segments of output co-sinusoidal signals from a Hall effect sensor, together with a simple and effective linearization technique. The theoretical absolute error of this converter is 0.05° over the full 360° range. In paper [5], a robust amplitude to phase converter, developed for the determination of position using the sine and cosine output signals of a resolver, is described. The theoretical absolute error in this case equals to 0.0082° over the full 360° range. However, the maximal absolute error obtained by applying the linearization circuit proposed in this paper (4-bit mixed-signal circuit and TSPLADC with N_1=4 bits and N_2=12 bits), equals to 0.00216° (3.77168·10^{-5} [rad]) over the full 360° (2π [rad]) range. As one can notice, in comparison to the result obtained in [6] the maximal absolute error obtained in this paper is more than twenty times lower, while in comparison to the result given in [5] it is four times lower. In addition, in papers [5] and [6] the information about the angle is obtained in analog format, while in this paper the angular position is converted into a digital format, which is very important since the majority of newly developed measurement systems are digital. Also, the linearization and digitalization are performed simultaneously by the same circuit, reducing in this manner the signal processing time, circuit complexity and its production costs and power consumption.

4. Conclusions

In this paper an improved solution of the optical rotary encoder linearization circuit is proposed. The proposed circuit is composed of the 4-bit mixed-signal circuit and the two-stage piecewise linear A/D converter. The advantages of the proposed linearization circuit are highlighted through a comparison with its previous version that is using the 3-bit mixed-signal circuit for the generation of pseudo-linear signal. Higher resolution in the mixed-signal circuit allows extraction of more linear fragments from co-sinusoidal signals, so that the pseudo-linear signal, which is further linearized in the two-stage piecewise linear A/D converter, has a better linearity from the start. The lower values of the maximal absolute error and of the nonlinearity, obtained after the application of the proposed linearization circuit, represent a significant improvement linked to the mixed-signal circuit resolution increase. The analysis of numerical results has shown that a greater impact on the absolute measurement

error reduction has the mixed-signal circuit resolution increase for one bit than the resolution increase of the first conversion stage, which is also performing the linearization. In other words, the linearization circuit with the 4-bit mixed-signal circuit achieves better results in comparison to the linearization circuit containing the 3-bit mixed-signal circuit and the first conversion stage with one bit higher resolution. In both cases the overall resolutions are the same. Therefore, it is more preferred to increase the complexity of the mixed-signal circuit instead of the complexity of the first conversion stage of the two-stage piecewise linear A/D converter.

The value of the maximal absolute measurement error, after the linearization is performed using the proposed circuit, equals to 3.77168·10^{-5} [rad] (0.00216°) over the full 2π [rad] (360°) range, which is two times lower in comparison to the corresponding parameter related to the linearization circuit of the same overall resolution that is employing the 3-bit mixed-signal circuit. Also, the solution proposed in this paper provides lower absolute measurement error in comparison to the analog linearization schemes given in the literature, which usually require an additional ADC for the applications in digital measurement systems.

References

[1] Ben-Brahim, L., Benammar, M., Alhamadi, M.A., Alemadi, N., Alhitmi, M. (2008). A new low cost linear resolver converter. *IEEE Sensors Journal*, 8 (10), 1620–1627.

[2] Ben-Brahim, L., Benammar, M., Alhamadi, M.A. (2009). A resolver angle estimator based on its excitation signal. *IEEE Transactions on Industrial Electronics*, 56 (2), 574–580.

[3] Benammar, M., Ben-Brahim, L., Alhamadi, M.A. (2005). A high precision resolver-to-DC converter. *IEEE Transactions on Instrumentation and Measurement*, 54 (6), 2289–2296.

[4] Benammar, M., Ben-Brahim, L., Alhamadi, M.A., Al-Naemi, M. (2008). A novel method for estimating the angle from analog co-sinusoidal quadrature signals. *Sensors and Actuators A: Physical*, 142 (1), 225–231.

[5] Benammar, M., Gonzales, A.S.P. (2015). Angular position measurement using resolvers together with a robust linearization technique. In *13th IEEE International Conference on Industrial Informatics (INDIN)*, July 22-24, 2015. Cambridge, United Kingdom. IEEE, 1510-1514.

[6] Benammar, M., Gonzales, A. Jr. (2015). Simple and precise analog arcsine synthesis applied to amplitude to phase conversion for Hall effect position sensors. In *6th International Conference on Sensor Device Technologies and Applications (SENSORDEVICES)*, August 23-28, 2015. Venice, Italy, 13-18.

[7] Lopez-Martin, A.J., Carlosena, A. (2013). Sensor signal linearization techniques: a comparative analysis. In *4th IEEE Latin American Symposium on Circuits and Systems (LASCAS)*, February 27-March 1, 2013. Cusco, Peru. IEEE, 1-4.

[8] Santos, M., Horta, N., Guilherme, J. (2014). A survey on nonlinear analog-to-digital converters. *Integration*, 47 (1), 12–22.

[9] Bucci, G., Faccio, M., Landi, C. (1997). The implementation of a smart sensor based on a piece-linear A/D converter. In *IEEE Instrumentation and Measurement Technology Conference Sensing, Processing, Networking (IMTC)*, May 19-21, 1997. Ottawa, Ontario, Canada. IEEE, 1173-1177.

[10] Bucci, G., Faccio, M., Landi, C. (2000). New ADC with piecewise linear characteristic: case study-implementation of a smart humidity sensor. *IEEE Transactions on Instrumentation and Measurement*, 49 (6), 1154-1166.

[11] Lopez-Martin, A.J., Zuza, M., Carlosena, A. (2003). A CMOS A/D converter with piecewise linear characteristic and its application to sensor linearization. *Analog Integrated Circuits and Signal Processing*, 36 (1), 39-46.

[12] Živanović, D., Lukić, J., Denić, D. (2014). A novel linearization method of sin/cos sensor signals used for angular position determination. *Journal of Electrical Engineering and Technology*, 9 (4), 1437-1445.

[13] Lukić, J., Živanović, D., Denić, D. (2014). Linearization method for angular position sensors. In *12th International Conference on Systems, Automatic Control and Measurements (SAUM)*, November 14-16, 2014. Niš, Serbia, 229-232.

[14] Lukić, J., Živanović, D., Denić, D. (2015). A compact and cost-effective linearization circuit used for angular position sensors. *Facta Universitatis, Series: Automatic Control and Robotics*, 14 (2), 123-134.

[15] Jovanović, J., Denić, D. (2016). A cost-effective method for resolution increase of the two-stage piecewise linear ADC used for sensor linearization. *Measurement Science Review*, 16 (1), 28-34.

[16] Fraden, J. (2010). *Handbook of Modern Sensors: Physics, Designs, and Applications*, New York, USA: Springer.

[17] Hamdy, N. (2008). *Applied Signal Processing: Concepts, Circuits, and Systems*, Boca Raton, USA: CRC Press.